Applied Thermal Engineering 290 (2026) 130128

Contents lists available at ScienceDirect

Applied Thermal Engineering

journal homepage: www.elsevier.com/locate/apthermeng

Research Paper

Numerical modeling of a deflagrative-based pressure gain combustor integrated with an axial turbine

C. Tempesti [a], S. Grasa [c], L. Romani [a,*], F. Ciccateri [b], G. Ferrara [a], G. Paniagua [c]

[a] Department of Industrial Engineering, Università degli Studi di Firenze, Via di Santa Marta 3, 50139 Firenze, Italy
[b] Finno Exergy Oy Ltd, Helsinki, Finland
[c] Zucrow Laboratories, Purdue University, 500 Allison Road, 47907 West Lafayette, IN, USA

ARTICLE INFO

Keywords:
Pressure gain combustion
Axial turbines
Turbomachinery design
Unsteady flows
Engine modeling

ABSTRACT

Pressure Gain Combustion (PGC) is a promising technology to significantly enhance the thermal efficiency of gas turbines by increasing stagnation pressure across the combustor. While most PGC research has focused on detonative-based systems such as Rotating Detonation Engines (RDEs), this study investigates an alternative deflagrative-based approach inspired by pistonless internal combustion engines. A comprehensive numerical analysis is presented, utilizing a dedicated simulation tool developed within the GT-Power environment to model the unsteady thermodynamic behavior of a deflagrative-based hydrogen-fueled PGC prototype. The combustor model was validated against high-frequency experimental data and then scaled to represent a real-engine application. To complete the system, a multi-stage axial turbine was specifically designed to accommodate the strongly pulsating outflow from the combustor. Despite significant fluctuations, the turbine maintained an average efficiency of 90% over the pulsation cycle. The combustor and turbine models were integrated into a full-cycle simulation framework, enabling the assessment of the complete system performance under transient operating conditions. The results indicate a cycle efficiency of 32.1%, representing a 7.7% improvement over conventional constant-pressure combustion systems. Despite being limited to a single operating condition, the modeling results are highly promising and provide a solid basis for future investigations. This work provides a viable alternative to detonation-based PGC technologies and shows potential for the feasibility of deflagrative-based systems for practical power generation applications. The modeling framework developed herein offers a scalable, computationally efficient tool for system optimization and supports further investigation of the proposed combustor concept.

1. Introduction

Pressure Gain Combustion (PGC) is a promising technology with the potential to considerably increase thermal efficiency, abate greenhouse emissions, and attain sustainable energy production. Due to the total pressure gain in the combustion chamber, this concept requires less compression upstream and less fuel burn, while providing an increased power/weight ratio over conventional Brayton cycles. The different typologies of pressure gain combustors can be classified into detonative and deflagrative-based. In deflagration-based technologies, the increase in stagnation pressure is due to the coupling of acoustic and thermal oscillation, like in Resonant Pulse Combustors (RPC) and Shockless Explosion Combustors (SEC), or to the management of input and output flows using mechanical or fluidic valves, like for Constant Volume Combustors (CVC). The combustor investigated in this manuscript is based on pistonless internal combustion engines. The pressure gain is created by the flow confinement inside the chamber, and the quasi-constant volume is generated by managing intake flows through controlled valves. A comprehensive description and operating principles were presented by Salminen et al. [1], where the fundamental concepts of the technology were outlined, and its feasibility was proven through preliminary experimental results. Subsequent research by Tempesti et al. [2] involved the experimental characterization of an updated prototype, fuelled with 100% hydrogen. The operational behavior of the system was captured via piezoelectric pressure measurements, providing valuable insights into the combustor's dynamics and validating its innovative features. Despite these significant contributions in prototype development and experimental testing, there remains a critical need for specific and detailed modeling of the system to better

---

* Corresponding author.
E-mail address: luca.romani@unifi.it (L. Romani).

https://doi.org/10.1016/j.applthermaleng.2026.130128
Received 5 June 2025; Received in revised form 23 January 2026; Accepted 3 February 2026

Acronyms

CFD	Computational Fluid Dynamics
CVC	Constant Volume Combustor
HTM	Heat Transfer Multiplier
ICE	Internal Combustion Engine
LES	Large Eddy Simulation
PDE	Pulse Detonation Engine
PGC	Pressure Gain Combustion
RANS	Reynolds-Averaged Navier-Stokes
RDC	Rotating Detonation Combustor
RPC	Resonant Pulse Combustor
SEC	Shockless Explosion Combustor
SST	Shear Stress Transport
STD	Standard Deviation
TPA	Three Pressure Analysis

Symbols

A	area [m^2]
D	mass flow function [−]
e	energy [J]
$\bar{f}$	reduced frequency [−]
f	frequency [Hz]
h	enthalpy [J/kg]
h_c	convective heat transfer coefficient [W/(m^{2}K)]
H	channel height [m]
L	length [m]
m	mass [kg]
$\dot{m}$	mass flow [kg/s]
M	Mach number [−]
n	normalization term [−]
obj	objective term [bar] or [−]
p	pressure [bar]
r	radius [m]
R	specific gas constant [J/kg K]
SF	scale factor [−]
$\overline{S_p}$	mean piston speed [m/s]
t	time [s]
T	temperature [K]
U	velocity [m/s]
V	volume [m^3]
w	weight term [−]
$\dot{W}$	power [W]

Greek symbols

α	absolute flow angle [deg]
β	relative flow angle [deg]
γ	specific heat ratio [−]
λ	air-to-fuel ratio over air-to-fuel stoichiometric ratio [−]
η_{tt}	isentropic turbine efficiency [−]

Subscripts

a	air
ax	axial
av	averaged
b	burned zone
f	fuel
i	injected
in	inlet
l	lambda
m	measured
mid	mid-span
out	outlet
p	pressure
s	simulated
u	unburned zone
0	total
1	turbine inlet
2	turbine vane outlet
3	turbine outlet

understand the technology.

Various modeling strategies can be found in the open literature, ranging from zero-dimensional to high-fidelity approaches. In 0D models, the pulsating nature of the systems is neglected, but it provides equivalent stationary states of combustion and expansion phases, making the comparison with conventional cycles simpler. Some of the most notable examples are the one of Nalim [3], who identified a modeling strategy to account for the partial expansion of gases in the combustor prior to entering the turbine, and Stathopoulos et al. [4], who refined this approach by introducing the effect of the secondary air system.

On the other hand, 3D Computational Fluid Dynamics (CFD) models offer a higher accuracy in capturing the detailed physical phenomena, at the cost of increased modeling complexity and computational cost. Labarrere et al. [5] and later Detomaso et al. [6] presented a fully compressible Large Eddy Simulation (LES) validated with experimental results for the development of a Constant Volume Combustor. In their system, flow confinement was attained through the management of intake and exhaust flows via both inlet and exhaust high-speed solenoid valves, with an architecture most similar to the one under investigation in the present paper. These analyses primarily focused on the valve characterization strategy, which constitutes the core of the system. For full-system analyses, the combustor geometry is typically simplified - for instance, by assuming a cylindrical shape. This approach is deemed suitable for SEC, Pulse Detonation Engines (PDE) [7], or RPC, where the combustor geometry consists of cylindrical tubes by design. However, for the configuration examined in this paper, such a simplification would have led to a considerable loss of accuracy.

In this context, 1D combustor models offer a practical compromise, being able to handle pulsating flows and thus ensuring a more accurate analysis than 0D models, without the complexity and cost of high-fidelity simulations. In the literature, for SEC, PDE, or RPC, 1D models are often based on the Euler equations solved in cylindrical-shaped combustion chambers. This approach avoids the need for more complex solvers while still capturing the process dynamics. Berndt et al. [8] applied 1D reactive Euler equations to a SEC, accounting for the reactivity of the mixture by including a balance equation for each chemical species present. The model enables the analysis of auto-ignition due to stratification, a fundamental and inherently unstable aspect of SEC processes. Neumann et al. [9] and Asli et al. [10] extended Berndt's work by incorporating the turbomachinery components – the compressor in the former and the turbine in the latter - into the same 1D unsteady inviscid solver. By employing energy and force source terms to simulate the blades' presence and their impact on the flow, this approach ensures that the transient conditions at the turbomachines' boundaries replicate some of the unsteady trends. The propagation of the flow unsteadiness across blade rows was analyzed and validated against 3D CFD results, indicating that the method effectively captures the transient behavior of the overall system and quantifies the attenuation of pressure fluctuations, achieving high accuracy at a very low computational cost. Nevertheless, this approach is only considered valid when the chamber geometry can reasonably be represented as a straight duct. Hence, its inability to handle more complex geometries makes it unsuitable for this study.

For the investigation of more complex geometries, alternative solvers are proposed. Sousa et al. [11] integrated the Method of Characteristics and turbine loss models to predict the performance of turbojets with a Rotating Detonation Combustor (RDC) and a supersonic turbine using NASA's T-MATS library. New libraries were implemented to model the RDC behavior and accurately replicate engine performances. Gallis et al. [12,13] used GT-power incorporating a parametrization of discharge coefficients, a modified non-dimensional burning rate, and a heat transfer model in a CVC. Their simulations matched experimental pressure fluctuations with acceptable accuracy. From existing literature, physics-based equation solvers are considered necessary when combustion chambers cannot be represented with cylindrical or duct shapes. In addition, the coupling with the turbine plays a critical role in the system [14–16]. Full-system modeling is essential for the precise quantification of its efficiency and operability, allowing for a proper assessment of its advantages over conventional systems.

This manuscript presents the development of a one-dimensional model of a deflagrative-based quasi-Constant Volume Combustor coupled with an axial turbine, aimed to assess the operability and the efficiency of the complete system under a representative operating condition. The novelty of the combustor's operating principle motivated the creation of a dedicated model within GT-power environment, given the system's similarities with internal combustion engines, and was validated with experimental data from tests conducted with 100% hydrogen. It is worth noting that this represents one of the first attempts to model a deflagration-based Pressure Gain Combustor of this kind within a one-dimensional framework. As such, the present work focuses on a single operating condition, and the proposed model is intended as a first-order approximation. While deviations from the reference operating point are expected and will require further investigation, the model provides an initial reference for evaluating system behavior and guiding future, more detailed developments of the proposed combustor concept.

Firstly, a model representing only the combustor was developed and calibrated using experimental results from previous activities [2]. The development of the combustor model and the calibration procedure are described in Section 3. Subsequently, the model was scaled up, and the transient conditions at the combustor outlet were used for the design of the downstream turbine. To provide a performance comparison to conventional power systems, an ad-hoc multi-stage axial turbine inspired by the TATEF turbine [17] stage was designed, following a combined 0D—3D approach to determine the turbine efficiency trend over a combustor pulsation cycle (Section 4). Finally, the individual component models were integrated into a single model, resulting in a global 1D model capable of evaluating the overall system performance. The work extracted along the pulsation was lastly compared with a Brayton cycle operating with the same input fuel power, resulting in a direct comparison with conventional and pressure gain architectures.

2. Constant volume combustion engine

The quasi-Constant Volume Combustor under investigation achieves a pressure gain during the combustion phase thanks to the chamber geometry and the management of the intake and exhaust flows. The concept is inspired by pistonless internal combustion engines. Timed valves on the intake control the scavenge and air/fuel intake while the outlet section is constantly open. Fig. 1 shows a scheme and a picture of the test bench. The combustion chamber comprises two sub-volumes in series connected by a restricted section. Henceforth, we will refer to the first and second volumes as “top” and “bottom” respectively. The upper portion of the combustor consists of a passenger car engine head, which actuates the opening and closing of the scavenging and intake poppet valves through a camshaft. These valves face directly into the top volume, where the mixture ignites. The bottom chamber is instead responsible for completing the combustion in a lean environment. For manufacturing issues, the combustor tested was composed of two twin elements in parallel.

Table 1
Controlled and acquired variables, with the reference point in the test bench and the corresponding sensor.

Point	Controlled Variables	Sensor type
C	Injection duration	All synchronized with the control unit through a Hall sensor
C	Injection timing	
D	Valve timing	
E	Ignition timing	
E	Pulsation duration	
Point	**Acquired Variables**	**Sensor type**
A	Ambient mean temperature	Type K thermocouple
B	Upstream dynamic pressure	Kulite XTL-123B-190 M
E	Chamber dynamic pressure	AVL GR14D
E	Mean wall temperature	Type K thermocouple
E	Ignition signal	Clamp meter
F	Exhaust dynamic pressure	Kulite EWCTV 312 (M)
F	Exhaust Lambda	Bosch LSU 4.9

The combustion process consists of four subsequent phases for each pulsation – combustion, exhaust, scavenging, and intake - that were characterized during the experimental campaign, detailed in [2]. At the start of the cycle, a controlled spark ignites the air/fuel mixture in the top sub-volume, and the flame front propagates throughout the chamber. Once it reaches the bottom sub-volume, the mixture completes the combustion in a lean environment. The fast flame propagation increases the temperature and pressure of the chamber gases. Since the outlet valve is not present, the pressure difference between the chamber and the exhaust drives the combustion gases through an opening section in the bottom sub-volume. When the chamber pressure is lower than the inlet air pressure, the scavenging valves open, letting fresh air enter the top sub-volume and scavenge combustion products. When the intake valves open, the air/fuel mixture refills the chamber, preparing it for ignition in the following pulsation. The discretization of combustion phases was done with respect to the chamber pressure trend and valve timing. It can be seen in Fig. 2, where the x-axis shows the dimensionless temporal discretization of one pulsation from 0% (=start, ignition) to 100% (=end). Triangular shapes represent scavenging and intake valve openings, while a rectangle indicates the injection period, and vertical dotted lines divide the phases. The phases are reported in the following order:

1. Combustion phase - from ignition to pressure peak.
2. Exhaust phase - from pressure peak to scavenging valve opening.
3. Scavenging phase - from scavenging valve opening to intake valve opening.
4. Intake phase - from intake valve opening to ignition.

3. Combustor analysis

This section describes the combustor one-dimensional model, validated with experimental data. The model layout faithfully recreated the test bench geometries and operating conditions used to acquire calibration data. Firstly, Section 3.1 describes the test bench layout and operating conditions of the tests, together with a general description of the corresponding model components. Then, Section 3.2 details the numerical setup, followed by the calibration strategy (Section 3.3). Lastly, Section 3.4 shows the scale-up approach.

3.1. Model layout

Strengthened by the parallelism with engines, the 1D model was implemented in GT-power [18,19]. It is a block coding software suited to model the entire combustion phenomena and specific for pulsating flows operating in internal combustion engines. To faithfully reproduce the

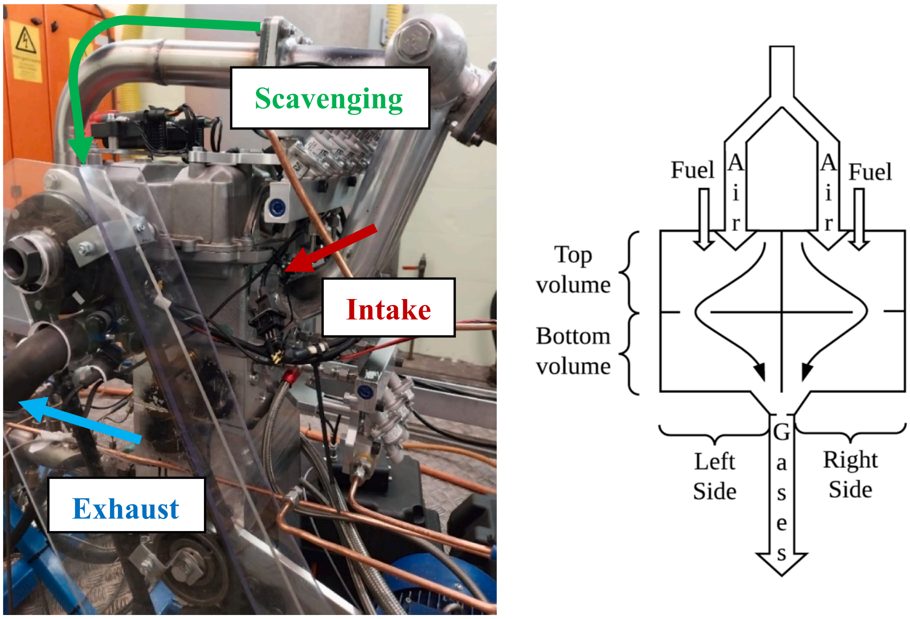

Fig. 1. Finno Exergy combustor. *Re*-adapted from [2].

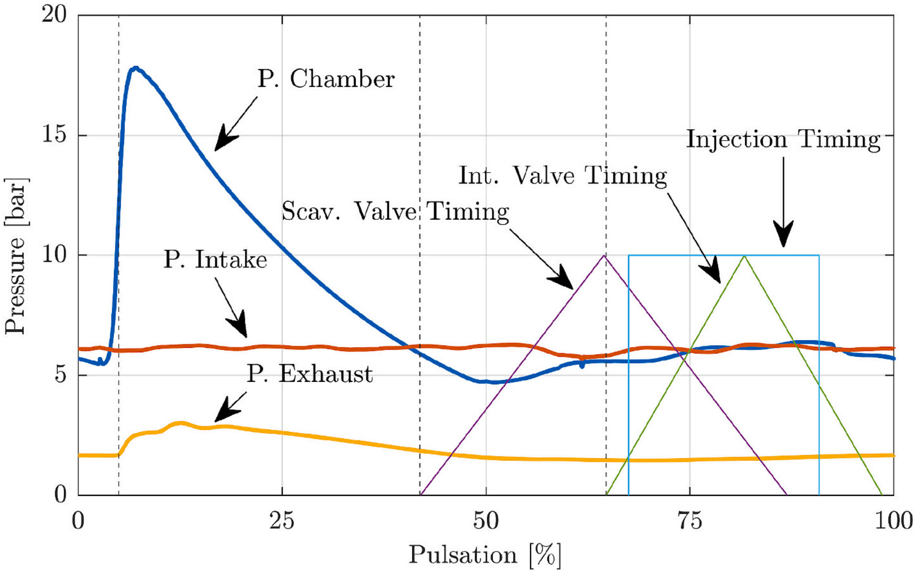

Fig. 2. Phases discretization, valve and injection timings. The spark is at 0%.

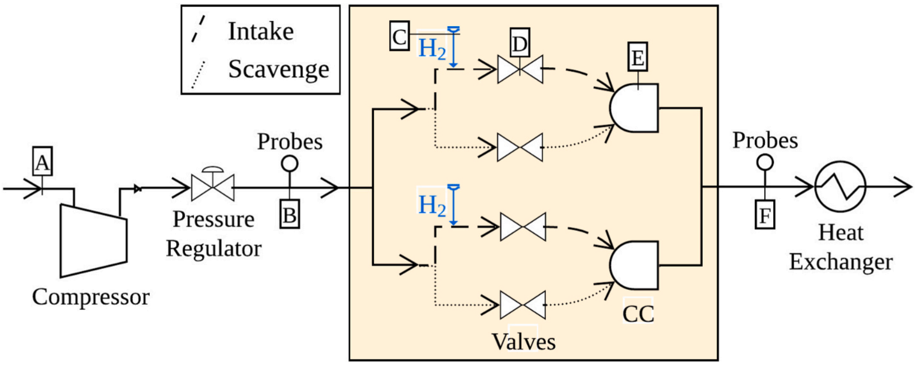

Fig. 3. Scheme of the test rig layout where experimental data was acquired, and variables acquired and/or controlled during the experimental campaign with the corresponding acquisition point, marked with letters from A to F. Controlled and acquired variables are listed in Table 1.

operating conditions of the test and ensure precise validation, the test rig - schematically shown in Fig. 3 - was modeled in detail. The intake air supply consisted of an air compressor and a pressure regulator, which served to set the air intake pressure. As mentioned earlier, the test bench comprised two parallel twin chambers. On each side, the fresh air line is split into two segments: the scavenge (dashed) and the intake (dotted) line. The intake line also served for hydrogen port fuel injection. Both scavenge and intake lines faced the chambers directly through a pair of poppet valves each. Consequently, each chamber had four poppet valves upstream, two for scavenging and two for air/fuel intake. The camshaft mechanism of the engine head actuated the valves' opening and closing. At the outlet section of each chamber, a calibrated orifice had the role of simulating the pressure drop across the turbine. Then, the outlets of the two chambers merged into the exhaust line, where a heat exchanger cooled the exhaust gases before discharging them into the ambient. The variables acquired or controlled during the experimental campaign are reported in Fig. 3 and served as input for the model. Among these, the pressure sensors at the intake (Kulite XTL-123B-190 M), in-cylinder (AVL GR14D), and exhaust section (Kulite EWCTV 312 M), as well as the lambda probe (Bosch LSU 4.9), were acquired at high frequency (1 MHz) via the AVL INDIMICRO acquisition system [2] to capture the dynamics correctly. The lambda value is an indicator frequently used for engine diagnostics. It represents the ratio between the tested and the stoichiometric air-to-fuel ratio. In the gas turbine community, it is common practice to refer to the equivalence ratio, which is defined as the reciprocal of lambda. Temperature values were instead acquired at low frequency (50 Hz) via K-type thermocouples. The upper section of the combustor was derived from a commercial passenger car engine head, including the original camshaft and poppet valves. The valve lift profiles were experimentally measured during the test campaign and directly imposed in the GT-Power model. The valve discharge coefficients were taken from the engine technical data sheet, as they correspond to the same hardware configuration used during the experiments.

Fig. 4 illustrates the model components of the described test rig, where the icons univocally refer to GT-power templates. The portion of the test bench recreated in the model is the one represented in the yellow square in Fig. 3, from the upstream to the downstream instrumentation section, where the experimental data acquired served as boundary conditions of the model (*BC-intake* and *BC-exhaust* blocks). The full detailed geometry of the rig was carefully reproduced; in the scheme, it is depicted for clarity by the only component *Upstream-geometry.* As in the test bench, each chamber had four upstream lines, two for the scavenging and two for the air/fuel intake. The port fuel injection was modeled by the *Injector1/2* components directly facing the intake line. All eight valves (*Vin1/2/3/4* and *Vsc1/2/3/4*) were modeled as cam-driven, defining their geometry and lift over one pulsation. The parallel combustion chambers were modeled as single cylinders with motionless pistons (*Chamber1/2*). At the chambers' outlet, the *Restrictor* templates represented the calibrated orifices of the test rig. Then, the two lines merged in the exhaust pipe, where the outlet boundary conditions were set. Specific details on all templates will be given in the following section.

3.2. Numerical set-up

Within the GT-power environment, the geometry of a system can be constructed by combining fundamental components, such as pipes and flow splits. The software also includes specific templates for engine applications like injectors, valves, and cylinders. These components are associated with established correlations and modeling approaches from the literature. Although the model architecture is well-suited to simulate a system that shares conceptual similarities with internal combustion engines, it still relies on a number of assumptions and simplifications that must be considered when interpreting the results. In particular, being a one-dimensional formulation, the model can capture phenomena such as pressure wave propagation, losses, reflections, and damping effects along the flow path. However, it cannot resolve spatial non-uniformities in species composition or temperature, which may play a role in more detailed representations of the combustor–turbine interaction. Nevertheless, the aim of the present work is to provide a framework for modeling and assessing the general operability of a deflagration-based Pressure Gain Combustor, rather than to achieve a high-fidelity prediction. Given this objective, the assumptions and simplifications introduced are considered acceptable.

The entire system is discretized into sub-volumes, where the

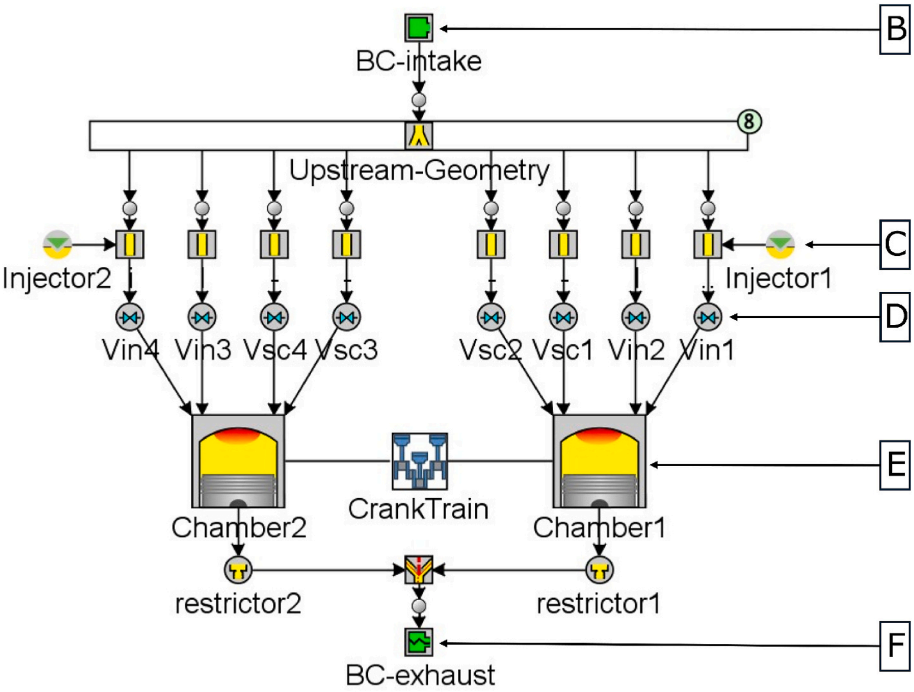

Fig. 4. Scheme of the model components replicating the test rig layout.

conservation of mass, momentum, and energy is solved in time and for one spatial dimension. The solver uses an explicit method with a staggered grid approach, computing the scalar variables in the volume centroids and the vector variables at the boundaries. The software operates in terms of cycles and crank angle-based quantities. The Pressure Gain Combustor under analysis was modeled as a 2-stroke engine, with one ignition event for each pulsation. Time-based quantities were converted into crank-angle based ones, with 0° representing the ignition event and 360° the pulsation duration. The engine speed was set to match the duration of one cycle with the tested pulsation duration. Hence, "cycle" and "pulsation" are used interchangeably, as each pulsation represents one cycle of a 2-stroke engine.

The typologies of templates available in GT-power and applied in the present model can be split into 4 categories: boundaries (*BC-intake* and *BC-exhaust*), pipes (which include everything in the *Upstream-Geometry* plus the pipes), flow connections (*Vin*, *Vsc*, and *restrictor*), and additional engine templates (*Injector*, *Chamber,* and *CrankTrain*). The geometry blocks can be discretized in sub-volumes by choosing their discretization length. For engine cycle simulation, a discretization length of 0.4 times the cylinder bore is recommended for the intake lines, and 0.55 times the bore is recommended for the exhaust. These values were used in the present test case. The other templates are instead treated as single volumes or boundaries. Inside these blocks, correlations are implemented to define an input-output relationship between variables, and will be detailed herein.

The boundary templates – *BC-intake* and *BC-exhaust* - define inlet and outlet boundary conditions of pressure, temperature, and fluid composition, all known from the experimental campaign.

The sequential pulse injectors (*Injector)* block was used for the port fuel injection modeling; it is typically used for spark ignition engines when the injection delivery rate [mg/cycle] and injection pulse width [ms] are known. The user can also specify the injection timing [deg] and the position in the pipe where injection occurs.

Flow connection templates include both valves and restrictors. They represent boundaries between the discretized volumes of the domain, where the momentum equation is solved to compute mass flow and velocity. Both scavenging (*Vsc*) and intake (*Vin*) valves were modeled using a cam-driven valve template, which defines the effective passage area based on the valve diameter and lift relative to the crank angle. The restrictors downstream each chamber (*Restrictor*), instead, were modeled with an orifice template, which connects two adjacent volumes by defining a diameter and a Discharge Coefficient (DC). The DC, derived from the isentropic velocity equation for flow through an orifice, is the ratio between the effective and the theoretical passage flow area.

Lastly, the coupling of *Cylinder* and *Cranktrain* blocks defines the engine's geometry and characteristics, with specific templates for detailed modeling on various aspects like combustion, heat transfer, in-cylinder flow, and scavenging. In ordinary GT-power applications, combustion occurs in *Cylinder* components, for which the *Cranktrain* element regulates the firing order, piston motion, and timings. The combustion chamber under investigation departs significantly from the ordinary layout, necessitating a unique approach to its analysis. Although it shares similarities with conventional engines, there are still deviations that could lead to inaccurate results if standard ICE templates are applied. This paragraph focuses only on the parameters and correlations identified as significant to the model's outcome. Additional analyses of other parameters that did not affect the response are excluded.

- Geometry: The chamber's internal shape is unique, consisting of two sub-volumes in series and lacking a piston. It was modeled using the engine cylinder template, with a volume equal to the sum of the two units' volumes. It is the framework within the software that allows pulsating combustion to be modeled, enabling the definition of all the associated mechanisms, such as combustion and heat transfer. To account for the piston's absence, it was kept stationary at the bottom dead center position.
- Scavenging: In 2-stroke engines, GT-power requires the definition of the scavenging function, which describes the in-cylinder mixing of incoming fresh gases with burned ones during the valve overlap period. By definition, it is the relationship between the cylinder and the exhaust residual ratio during intake and exhaust valve overlap. The residual ratio compares the burned gas mass to the total gas mass, with the cylinder residual ratio concerning the cylinder volume and the exhaust related to gases exiting the cylinder. Mathematically, the scavenging function is described by three parameters: the shape factor, the anchor point, and the transition point (Fig. 5). The shape factor controls the profile curvature; increasing the shape factor increases the curvature. The anchor point is the cylinder residual ratio value at which the exhaust residual ratio is 0.5. The transition point is the lowest cylinder residual ratio for which the exhaust residual ratio equals 1.0. In our case, the process deviated from the conventional scavenging phase occurring in two-stroke engines due to the absence of exhaust valves. Consequently, we had no information on the scavenging function, leaving all three parameters unknown.
- Heat Transfer: Accurately capturing Heat Transfer (HT) is crucial for proper modeling, as incorrect values can alter the conservation of energy. In the software, heat transfer is represented through the combination of two elements: a cylinder wall boundary condition and a correlation-based model for evaluating the convective heat transfer coefficient within the chamber. Firstly, we had to match the combustion chamber area where HT occurs. Having modeled the chamber as an engine-cylinder, its internal surface differed significantly from the actual one, and it required adjustments. To do so, the Head/Bore and Piston/Bore area ratios were adjusted so that the simulated and tested HT surfaces matched each other. These parameters are applied in engine simulations to account for the head and piston areas in engines. From the experimental campaign, three measured quantities were available to support the evaluation of heat losses: the average chamber wall temperature, the average exhaust gas temperature, and the heat rejection through the cooling water. The first two were directly applied in the heat transfer modeling. The measured chamber wall temperature was imposed as the in-cylinder wall boundary condition, while the exhaust gas temperature was used as a constraint during the calibration process; more of this will be explained later. The cooling water heat rejection was available only as an order-of-magnitude estimate and was therefore used at the end of the simulations to verify that the predicted total heat losses were of the correct magnitude. Then, the HT model had to be chosen. In ICE applications, modeling the HT coefficient commonly involves, among other parameters, the average in-cylinder gas velocity. The Woschni correlation is globally recognized and most widely applied in conventional cases. Indeed, in GT-power, most of the HT models implemented are based on the Woschni correlation or its variants. For these models, the average in-cylinder gas velocity is a function of the displaced volume and of the piston mean speed. Both these variables were null in our test case since the piston was motionless; therefore, applying these models would result in extremely low heat losses. The only available model that employs a different approach is the Hohenberg correlation [18], which computes the HT coefficient via the following relationship:

$$h_{c,H} = 130 \cdot V^{-0.06} \left(\frac{p}{10^5} \right)^{0.8} T^{-0.4} \left(\overline{S}_p + 1.4 \right)^{0.8} \tag{1}$$

Here $h_{c,H}$ is the convective heat transfer coefficient computed via Hohenberg correlation, V, p and T are cylinder volume, pressure in Pascals and temperature, and $\overline{S}_p$ is the mean piston speed. The mean piston speed also appears in the Hohenberg correlation, but it does not nullify the term thanks to the inclusion of the value 1.4 in the final term. However, this formulation was originally derived for

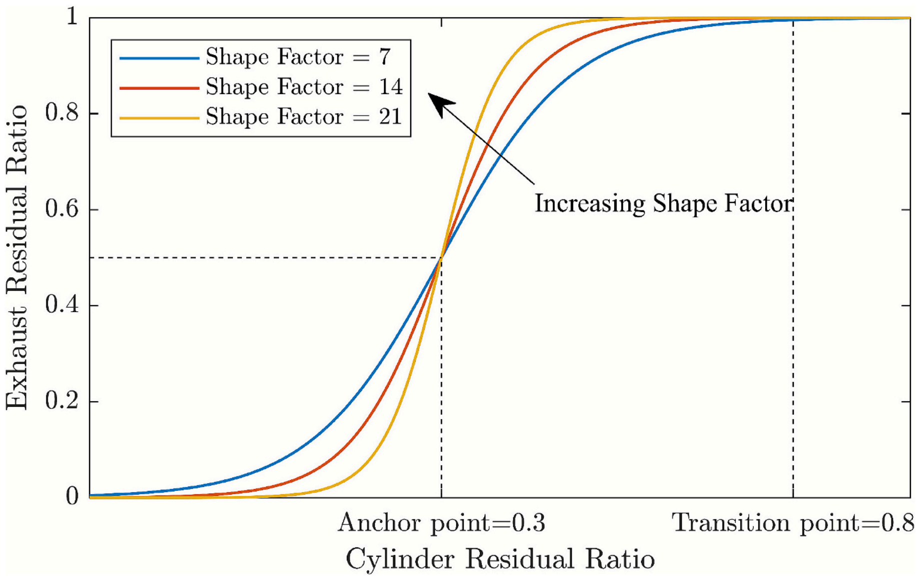

Fig. 5. Representation of scavenging function parameters.

ICEs, and the heat transfer characteristics of the combustor under investigation may differ; the correlation was used here primarily as a mathematical framework to include a physically reasonable level of heat losses. Still, the amount of heat transferred could be underestimated due to the dependency on the mean piston speed. To account for it, the Heat Transfer Multiplier (HTM) could be adjusted. It is a corrective factor that varies the convective heat transfer coefficient, as shown in Eq. 2.

$$h_c = HTM \cdot h_{c,H} \tag{2}$$

Changing the HTM changed the energy balance and, apart from the temperature, it also affected the pressure trace inside the chamber.

- Combustion: GT-power models combustion using a "Two-Zone" approach, which divides the cylinder into two parts - an unburned and a burned zone. At ignition, all the cylinder contents belong to the unburned zone. At each time step, the burn rate determines the fuel consumption rate and consequently quantifies the amount of the air-fuel mixture transferred from the unburned to the burned zone. A chemical equilibrium calculation of the burned zone updates the composition and energy of the combustion species. The new unburned and burned zone temperatures and cylinder pressure are thus obtained. At each time step, Eqs. 3 and 4 are solved for the unburned and burned zones, respectively:

$$\frac{\mathrm{d}(m_u e_u)}{\mathrm{d}t} = -p\frac{\mathrm{d}V_u}{\mathrm{d}t} - Q_u - \left(\frac{\mathrm{d}m_{f,b}}{\mathrm{d}t}h_f + \frac{\mathrm{d}m_{a,b}}{\mathrm{d}t}h_a\right) + \frac{\mathrm{d}m_{f,i}}{\mathrm{d}t}h_{f,i} \tag{3}$$

$$\frac{\mathrm{d}(m_b e_b)}{\mathrm{d}t} = -p\frac{\mathrm{d}V_b}{\mathrm{d}t} - Q_b + \left(\frac{\mathrm{d}m_{f,b}}{\mathrm{d}t}h_f + \frac{\mathrm{d}m_{a,b}}{\mathrm{d}t}h_a\right) \tag{4}$$

Here, subscripts "u", "b", "f" and "a" indicate unburned, burned zone, fuel, and air, respectively; subscripts "f,b" and "a,b" indicate fuel and air transferred to the burned zone; subscript "f,i" indicates fuel injected. The terms Q_u and Q_f denote the heat transfer rates in the two zones, modeled according to the heat transfer formulation described earlier. The term $\frac{\mathrm{d}m_{f,b}}{\mathrm{d}t}$ is the burn rate, the instantaneous fuel consumption rate. It is a pivotal parameter, being the discriminant between predictive and non-predictive combustion models. A non-predictive combustion model sets a burn rate as a function of the crank angle, either by directly imposing the combustion profile or applying well-known engine combustion models. In contrast, for a predictive combustion model, the burn rate is an output; it is typically used when the variables of interest have a direct and significant effect on the burn rate. For the present test case, a Three Pressure Analysis (TPA) – a predictive combustion model – was applied. This method is widely used in engine simulations as pressure can be acquired with high temporal resolution and serves as the primary diagnostic variable. It requires measurement data for its calibration, specifically the upstream, chamber, and exhaust dynamic pressures, which the solver matches by varying the burn rate.

3.3. Calibration strategy

From the numerical layout, six model variables remained unknown: the scavenging function parameters – shape factor, anchor point, and transition point – the mass of hydrogen injected per cycle, the Discharge Coefficient of the restrictor, and the Heat Transfer Multiplier. The calibration strategy aimed to identify these unknown parameters. All the acquired variables served as model inputs in the various templates. Both lambda and pressure trends were influenced by the calibration parameters, with lambda showing higher sensitivity than pressure. Thus, a multi-objective optimization strategy was defined, aiming to match the in-cylinder pressure and the exhaust lambda trends over one pulsation. To do so, the solver tried to minimize the standard deviation (STD) between the measured and simulated pressure and lambda trends over one pulsation:

$$obj_p = \sqrt{\frac{\sum_i^N (p_m - p_s)_i^2}{N}}; \quad obj_\lambda = \sqrt{\frac{\sum_i^N (\lambda_m - \lambda_s)_i^2}{N}} \tag{5}$$

Here, subscripts "m" and "s" refer respectively to measured and simulated, and N is the number of discretized intervals over one cycle. The choice of the parameter bounds depended on the physical meaning and formulation of each parameter. Three out of the six parameters – namely the anchor point, transition point, and Discharge Coefficient - are predefined within the software, with allowable values ranging from 0 to 1. The Heat Transfer Multiplier is also predefined, with limits between 0 and 5. The shape factor, instead, was limited to 100, as higher values were found to have negligible influence on the scavenging function shape. For the hydrogen mass injected per cycle, the experimental measurements provided an indication of its order of magnitude.

Preliminary runs were performed with the optimizer to verify that the imposed limits were appropriate. In subsequent runs, the bounds were progressively narrowed to guide the optimizer toward better convergence and more physically meaningful results. Depending on the outcomes, additional constraints were introduced in the optimization process to ensure the results closely matched the actual experiments. The first one limited the exhaust temperature to below 700 °C, a value consistent with the experimentally measured average exhaust gas temperature; the second one forced the minimum simulated lambda value during a pulsation between 1.4 and 1.55, based on the actual measured minimum value of 1.47. These constraints were necessary because preliminary analyses showed that, without them, the solver converged to values that did not accurately reflect the experimental conditions.

For the present test case, two main optimization approaches could be applied: a weighted sum or a Pareto front. The former combines the objectives by making use of weights and normalization terms; it creates a single objective function, resulting in a single optimized layout. Conversely, the Pareto approach searches for as many Pareto optimal designs as possible rather than aiming to find the single best design. When a single optimal design is required, as in the activity reported herein, a weighted sum algorithm is typically advised. However, for the present test case, it was not possible to normalize or assign the desired weights to the two objective functions. Therefore, an unconventional methodology was developed by mixing these two approaches.

Firstly, the multi-objective optimization solver with the Pareto front approach and Genetic Algorithm was employed. The software uses the NSGA-III evolutionary algorithm [20], implemented via the open-source, Java-based MOEA Framework [21]. Further details about the algorithm and its implementation are provided in the cited references. With two objectives, six factors, and two constraints, the population size had 26 items. The solver automatically computed 15 generations. Since a significant percentage of results from the first 15 generations violated the constraints (43.6%), 30 generations were added. After completing 45 generations and 1170 designs, the solver identified 135 layouts belonging to the Pareto front. Fig. 6 illustrates these results, where the blue points represent design points, and the red ones denote the designs belonging to the Pareto front. The image is zoomed in to provide a clearer view, and the designs furthest from the Pareto front are not shown. The x and y axes correspond to the first and second objective functions, namely the STD of the pressure and lambda trend. Without normalization, the two objective functions for the 135 Pareto front designs exhibited values significantly different from each other, with the mean lambda STD being almost six times that of the pressure. A graphical representation is shown as an example in Fig. 7 for 15 Pareto designs. Applying a weighted sum algorithm from the beginning would not have allowed us to know a priori how much each objective would influence the total. Therefore, the normalization was performed a posteriori. The objective functions, even if similar mathematically, had different units of measure and order of magnitude. Thus, instead of performing a physical normalization, a mathematical one was done. The normalization terms were computed as follows:

$$n_i = \frac{\overline{obj_i}}{\overline{obj_p} + \overline{obj_l}} \qquad \text{with} \quad i = p, \lambda \tag{6}$$

Where $\overline{obj_i}$ are the means of the objective functions over the 135 Pareto designs. With this mathematical normalization, the objective functions of the 135 Pareto designs have the same effect in absolute value and can be summed up in a single objective function. If necessary, the user can assign a weight to each objective to prioritize one objective over the others. The global optimization function would then be computed by a classical weighted sum:

$$f = \min\left(w_p \frac{obj_p}{n_p} + w_l \frac{obj_l}{n_l}\right) \tag{7}$$

Fig. 8 and Fig. 9 show the results in terms of pressure and lambda trace over a pulsation. The pressure trace closely follows the measured signal, except for the peak value, which the simulation overestimates by 3.2%. The reason may be influenced by a series of contributions. Firstly, due to the discrepancies in the combustion chamber shape between the model (cylindrical) and the one tested. The chamber's internal shape is optimized to confine the flow sequentially in two sub-volumes in series, and the software does not correctly capture the dynamics occurring. More importantly, variations in the burn rate profile and in the calibration factors have a direct influence on the pressure curve and on the peak pressure magnitude. In principle, a reduction of the pressure peak could be achieved by modifying the burn rate evolution or the calibration factors. However, in the present work, the burn rate shape and the model calibration coefficients were obtained through a global optimization procedure aimed at simultaneously matching the entire chamber pressure trace and the exhaust lambda evolution. Once this global optimum was reached, alternative combinations of burn rate profiles and calibration coefficients could potentially yield a closer match of the pressure peak value, but at the expense of a worse agreement during other phases of the combustion process or a of the lambda simulated trend. Additionally, it should be noted that the experimental pressure

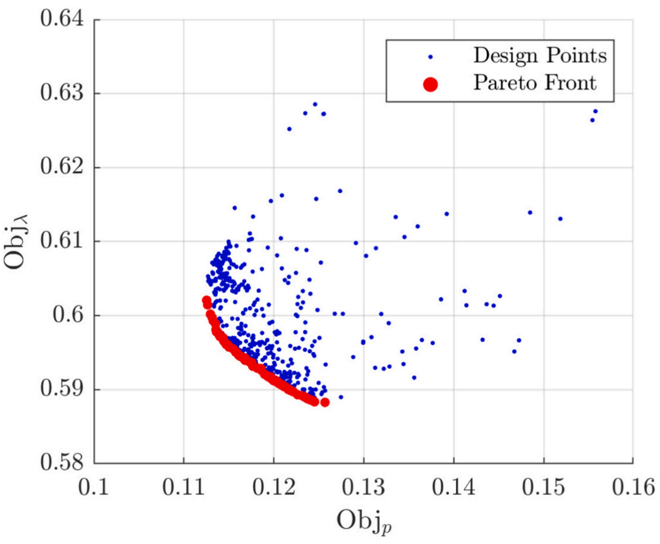

Fig. 6. Results of the multi-objective optimization.

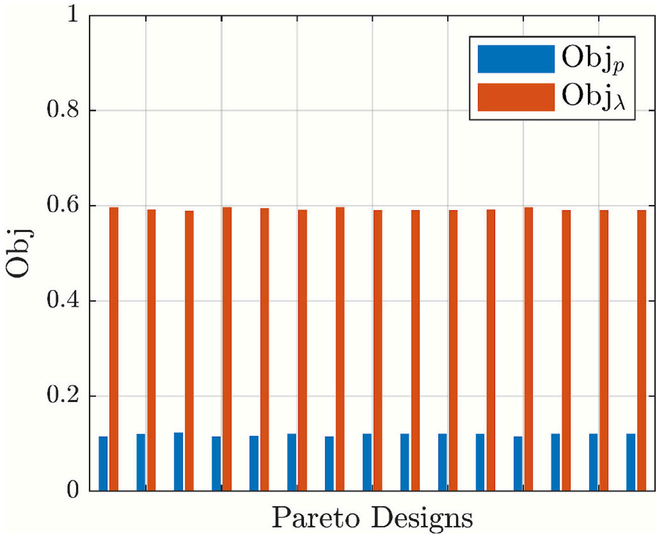

Fig. 7. Visual representation of the difference in absolute value between the two objective functions.

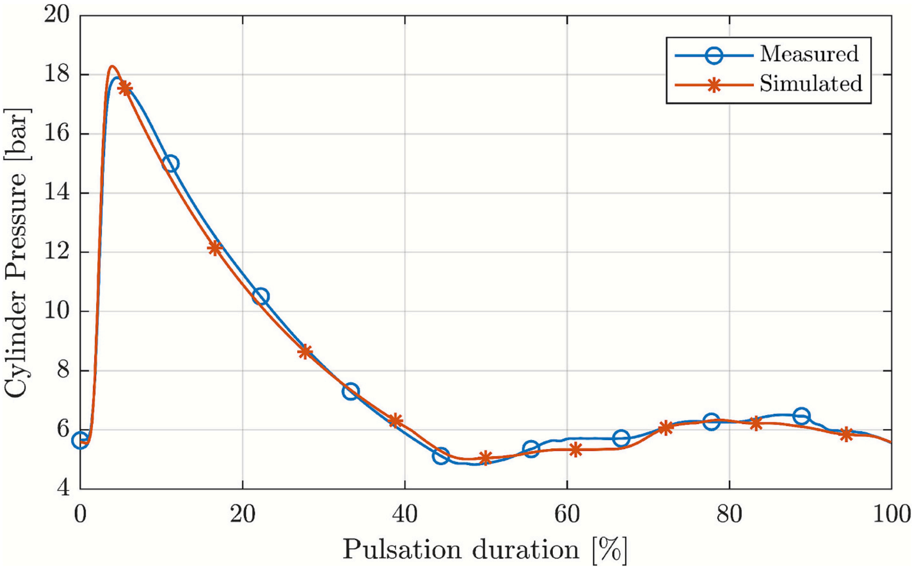

Fig. 8. Measured and Simulated chamber pressure traces.

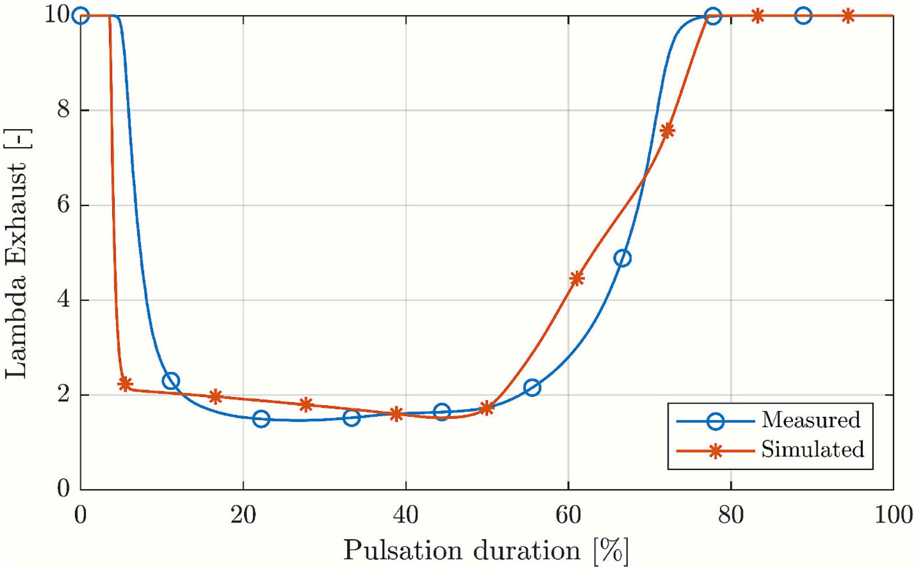

Fig. 9. Measured and Simulated exhaust lambda traces.

measurement at the pressure peak is affected by an uncertainty of approximately ±2.1% of the measured value. When this uncertainty is taken into account, the discrepancy between simulated and measured peak pressure at its upper bound of uncertainty is reduced to 1.0%. A direct and rigorous quantification of the impact of these deviations on combustion efficiency remains challenging within the current modeling framework. Nevertheless, a quantitative assessment can be provided. In particular, in the region close to the pressure peak, where the simulated pressure trace exceeds the measured one, the excess area under the pressure curve, which can be interpreted as an indicator of released energy, accounts for approximately 4% of the total integrated area over the cycle. This contribution is therefore limited and suggests that the associated impact on the overall energy release, and consequently on combustion efficiency, is not significant. In,addition, given the approximations in the modeling, the accuracy is adequate for the validation.

Regarding the lambda, the deviation is higher. The solver captures the main trend: the lambda value decreases during the combustion phase and eventually reaches a minimum value of 1.52, even if with a delay compared to the measured trace. The main deviation involves the derivative of the curves during the exhaust phase: the simulated trend shows a rapid decrease at 3.6% of the pulsation, quickly reaching a value close to 2 before gradually decreasing to 1.52. In contrast, the measured trace has a lower derivative, beginning its gradual descent from 4% of the pulsation and decreasing more gently to a minimum value of 1.47. Given that the software is specialized solely for ICEs, the level of agreement is deemed acceptable. The possible reasons that could cause these deviations are explained herein. Firstly, they may be due to the absence of the exhaust valve. In ordinary engine operation, burned gas exits the cylinder as soon as the exhaust valve opens, causing the lambda trend to decrease rapidly. In our test case, the outlet section of the chamber is constantly open, allowing burned gases to exit continuously. In addition, the chamber shape is crucial in restricting the flow: the mixture burns in a rich environment in the top sub-volume and completes the combustion only after reaching the bottom sub-volume. This operational characteristic may contribute to a less steep curve of the measured trace. Another approximation arises from the scavenging function: in conventional operation, it is defined during the valve overlap period. Due to valve absence and chamber shape, the real thermo-fluid dynamics occurring inside the chamber are likely different. In addition, the primary cause of the deviation between measured and simulated values may come from the lambda sensor's operational functioning. The Bosch LSU 4.9 sensor uses two cells for its functioning - a reference and a pump cell – and a measurement cavity. The reference cell is kept at stoichiometric conditions by monitoring and adjusting its voltage to a setpoint value. A deviation in the reference cell's potential indicates a deviation in the oxygen partial pressure from stoichiometric conditions in the measuring cavity. The pump cell then pumps oxygen in or out of the cavity to restore the reference conditions. Under typical engine conditions, the probe is used for steady measurements as its response time is declared to be around 50 ms. Exact values are not specified by the producer, since its actual response time varies depending on the operational conditions of pressure, temperature, and cycle frequency. However, Regitz [22] analyzed the sensor response time and reported values between 5 and 25 ms. In the present test case, the operational frequency of the combustor was the equivalent of 700 rpm, way less with respect to a common engine. Thus, the authors are confident that the sensor can capture the dynamics, even with some delays. If the sensor does not reach equilibrium in the cells before each sample point, the probe response operates by doing a moving average with the exhaust gases that pass from the measurement cavity. This causes a small delay and smoothness of the curve. Given all the limitations of the model and of the software to correctly capture the actual phenomena, the authors consider the calibration valid, since the global trend is captured.

The calibration parameters are reported in Table 2. To verify the robustness and reproducibility of the calibration, the optimization procedure was repeated three times using different random seeds for the Genetic Algorithm while keeping all other settings unchanged. The optimizer consistently converged to parameter sets within the same range, confirming the stability of the identified solution. In the table, the column *Reference Calibration* reports the parameter values obtained from the baseline optimization, which were adopted in all subsequent simulations. The columns *Validation Run #1* and *Validation Run #2* show the corresponding results from two additional independent optimizations performed with different random seeds, illustrating the good repeatability of the calibration process.

Although the heat transfer surface area was geometrically matched to the experimental configuration through the Head/Bore and Piston/Bore ratios, an additional sensitivity analysis was performed to assess the robustness of the model with respect to minor surface area variations. The heat transfer area was varied by ±5% with respect to the reference value, while all other model parameters were kept unchanged. The impact of these variations was evaluated using the objective functions obj_p and obj_λ. An increase of the heat transfer surface area by 5% resulted in a 0.25% increase in obj_p and a 0.06% increase in obj_λ. Conversely, a decrease of the surface area by 5% led to a 0.79% reduction in obj_p, while obj_λ increased by 0.05%. These results indicate that moderate deviations in the heat transfer surface area have a negligible influence on the model predictions.

Table 2
Calibration parameters.

Calibration Parameter	Reference calibration	Validation Run #1	Validation Run #2
Hydrogen mass per cycle [mg/cycle]	37.56	37.89	37.77
Discharge Coefficient restrictor [−]	0.97	0.97	0.97
Heat Transfer Multiplier [−]	3.89	3.90	3.90
Shape factor [−]	97	85	90
Anchor point [−]	0.46	0.46	0.46
Transition point [−]	0.80	0.83	0.86

With this methodology, it was possible to obtain a single optimized layout despite starting from a multi-optimization problem. It is a valid and straightforward approach, suitable also for more complex problems involving multiple objective functions, especially when normalization is critical. By simplifying the optimization process while maintaining accuracy, this method could be adaptable and effective for a wide range of applications. In the test case reported herein, a calibrated model of a non-conventional engine was obtained, validated with experimental data.

The results presented in this work are specific to the investigated combustor and to a fixed operating condition. In particular, the model is based on an operating frequency of 12 Hz and on prescribed injection, ignition, and valve timings, which are not disclosed in detail due to intellectual property constraints. The system dynamics are characterized by the measured evolution of pressure upstream the combustor, within the combustion chamber, and downstream of the combustor, as well as by the exhaust lambda. A such, the present modeling effort represents a first order validation of the proposed concept. Further investigations will be required to assess the predictive capability of the model under off-design and alternative operating conditions, and to evaluate its robustness in capturing deviations from the reference case. Nevertheless, the modeling methodology presented herein is not limited to the system analyzed. With appropriate adjustments to geometric representations, boundary conditions, and operating logic, the proposed approach can be extended to the modeling of other deflagrative-based quasi-Constant Volume Combustors.

3.4. *Turbine sizing impact on the combustor operation*

A key challenge in PGC systems lies in evaluating and quantifying the turbine's efficiency when subjected to pulsating flow, as reported in the literature [14–16]. The primary goal of the activity was thus to assess how effectively the combustor could be integrated with a downstream turbine. The pressure gain combustion system is aimed at industrial gas turbines for power generation, in the range from 1 to 100 MW. However, the fuel power of the current prototype is around 200 kW. To simulate the performance of an industrial gas turbine equipped with the pressure gain combustion system, the combustor model must be scaled up. The geometric and operating turbine properties were known and will be detailed in the following section. The scale-up model reported herein is a simplified, preliminary attempt to assess the system's potential and evaluate its performance.

The test rig used to examine the combustor operation had limitations on the amount of energy injected into the system, with the fuel line being its bottleneck. In both the experimental prototype and the corresponding validated model, a calibrated orifice at the combustor outlet ensured proper functioning by generating a choked point in the system. Experimental results used for model validation were obtained with an 8 mm diameter orifice. When testing with increased restrictor diameters, the fuel line pressure dropped, indicating it couldn't supply the desired amount of hydrogen per cycle. Thus, before proceeding with the scale-up, the calibrated model served to simulate the combustor's operation with a larger restrictor diameter. This adjustment was necessary to prevent an excessively large ratio between combustor volume and outlet passage area, which would result in a scaled-up combustor with an unnecessarily large volume for practical applications. The tested orifice diameter of 8 mm was increased to 12.5 mm for the simulation, as it ensured analog choking conditions. Due to the growth of the outlet section, the operational frequency was also raised to match the validated burn rate. With a larger restrictor diameter, higher air and hydrogen mass flows are processed; increasing the frequency ensures a chamber pressure trace that follows closely that of the validated model from ignition to exhaust phase (Fig. 10). The phenomena occurring inside the chamber during the combustion and exhaust phases are matched. A

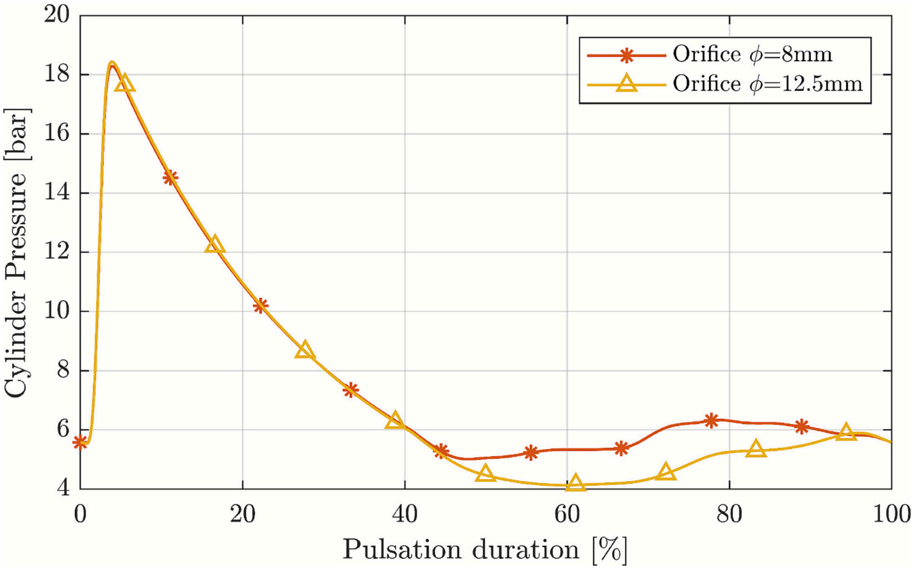

Fig. 10. Chamber pressure of validated model with 8 mm restrictor diameter (red star curve) and model with 12 mm restrictor diameter (yellow triangle curve). (For interpretation of the references to colour in this figure legend, the reader is referred to the web version of this article.)

higher deviation is observed during the scavenging and intake phases. This indicates that the current test bench would not be adequate to supply the necessary airflow to maintain the chamber pressure equal to the intake value during upstream valve opening, causing the chamber pressure to drop below the intake pressure during valve opening. Increasing the valves and pipes' diameter by 30% restored realistic operating conditions also in the intake phase. For the purposes of this study, this setup is sufficient, and the scaled-up model was thus developed based on the 12.5 mm restrictor diameter model.

To establish the boundary conditions at the turbine inlet with the scaled-up combustor, a similar combustor model was developed. It accounted for the presence of an actual turbine by recreating the subsequent pressure drops encountered by the flow exiting the combustor.

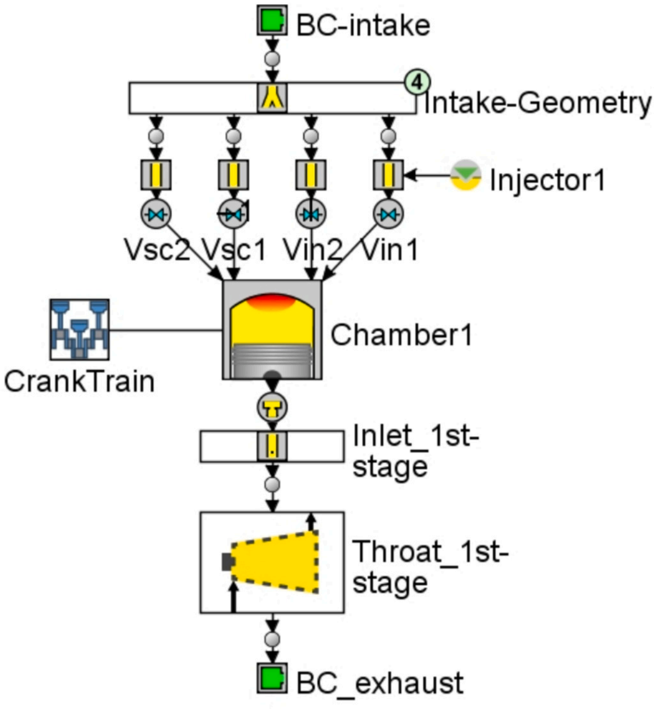

Fig. 11. Scheme of the scaled-up model.

Fig. 11 shows the model layout that most accurately represented the real setup and allowed it to match the desired conditions. At the combustor exit, a *Pipe* and a *Turbine* GT-power block represent the 1st stage stator inlet and throat, respectively, named *Inlet_1st-stage* and *Throat_1st-stage* in the scheme. The *Turbine* GT-power block is a simplified turbomachinery template, typically used to model turbochargers, that predicts the power, mass flow, and outlet temperature using an orifice flow model with an imposed turbine isentropic efficiency. It is worth noting that, at this stage, the turbine is represented through a simplified template (GT-Power 'Simple Turbine') with a constant isentropic efficiency. This approach is adopted to impose a realistic backpressure and to obtain first-order estimates of the thermodynamic boundary conditions at the turbine inlet, needed for subsequent turbine simulations. The unsteady behavior of the turbine efficiency under pulsating inlet flow is not captured in this initial model; however, a refined representation using an efficiency profile varying over the pulsating cycle, derived from CFD analysis, is introduced and discussed later in Section 5.

The Scale Factor (SF) is defined as the ratio between the first turbine stator throat area, corresponding to the scaled-up model, and the area of the exhaust restrictor, where flow choking was observed. The choice of these specific parameters was driven by the occurrence of choked flow in both sections. The turbine is fed by 24 combustors; hence, the reference area for the scaled-up system should be 1/24 of the full annulus throat area, as indicated in Eq. 8. Using 24 combustors allows a limited scale-up of each unit, avoiding excessively large combustor volumes and enabling a scaling that is not too large from the tested prototype.

$$SF = \frac{\frac{A_t}{24}}{\frac{\pi \cdot 12.5^2}{4}} \tag{8}$$

With the use of these parameters, the scale factor ensures an accurate reflection of the dynamics at the crucial point of flow restriction. From the exhaust section, all upstream geometric variables can be scaled accordingly: the one-dimensional variables – such as pipe diameters and valve lift – were scaled with the SF, while the chamber volume was scaled with the SF cubic power. The pulsation frequency was initially reduced by a factor of 1/SF, in accordance with common engine scaling laws, and then adjusted to synchronize the end of the exhaust phase with the scavenging valve opening.

Like the model with a 12.5 mm restrictor diameter, the scaled-up model exhibited a chamber pressure drop during the upstream valve opening, compared to the intake value. This indicated that the intake line was incapable of supplying the necessary amount of air to properly fill the combustor. To address this issue, the diameters of the valves and intake pipes were increased by 30% as before, ensuring that the chamber pressure remained equal to the supply value during the upstream valve opening. Finally, the intake pressure and the hydrogen mass flow were fine-tuned to match the required turbine intake conditions of pressure and temperature, respectively. The pressure, temperature, and mass flow trends over a pulsation at the combustor outlet serve as inlet boundary conditions for the turbine design, discussed in Section 4. Due to the limited amount of data available, insufficient for the construction of more refined models, a finer representation of the system was not pursued at this stage. The scaled-up model allowed us to retain the transient conditions at the combustor outlet, specifically in correspondence of the component Inlet_1st-stage in the scheme in Fig. 11, in terms of mass flow, temperature, pressure, and composition. These conditions are crucial for evaluating turbine design and efficiency along a pulsation.

4. Turbine design methodology

To maximize the potential cycle-level benefits of pressure gain technologies, the turbine geometry must efficiently handle the fluctuating conditions at the combustor exhaust, which strongly differ from conventional gas turbines. As shown by Liu et al. [15], different perturbation amplitude levels at the turbine inlet can lead to a turbine efficiency abatement of up to 12 percentage points. Additionally, unsteady, highly subsonic, or transonic inlet Mach numbers may require tailored turbine designs to effectively ingest the combustor outflow [23]. This chapter describes the design methodology of a multi-stage axial turbine, suited to the pulsating flow provided by the deflagrative-based pressure gain combustor.

4.1. Turbine inlet conditions

The analysis of the boundary conditions is the first step in the design of the turbomachine. This provides information about the required range of operation and informs the sizing and the selection of the most suitable architecture. Furthermore, the intensity of the inlet fluctuations determines how tolerant the design should be to off-design conditions. To ensure a mixed-out axial flow at the turbine inlet, the transition duct between the combustor and the turbine will be designed to dampen any vortical structures induced by the valve actuation at the combustor inlet. As a result, the turbine inlet boundary conditions are retrieved from the one-dimensional scaled-up combustor model and are illustrated in Fig. 12 in terms of total pressure, total temperature, specific heat ratio, and gas constant, for a single pulsating period. The downstream static pressure is set to sea-level atmospheric. The system's operating frequency is 10 Hz, leading to a pulsating period of 0.1 s.

Given the intense unsteady flow downstream of the combustor, off-design turbine operation is expected for most of the pulsating period. Nevertheless, a reference set point is needed to perform the turbine sizing, selected based on the boundary conditions available prior to the design phase, presented in Fig. 12. Two metrics are considered to determine an adequate design point. First, the pressure ratio, defined as the quotient between the inlet total pressure and the outlet static pressure. As the pressure ratio drifts away from the on-design value, the turbine efficiency is abated. Hence, choosing an intermediate pressure ratio value along the time-dependent profile as the on-design point may lead to superior efficiency over the entire pulsating period. From Fig. 12, the highest and lowest pressure ratios are 13.5 and 6, respectively. Thus, a design value in the order of 9.5 may result in a good compromise.

Moreover, to maximize the overall performance, it is vital to study the evolution of the available power for the time-dependent set of inlet conditions, recognizing that greater efficiencies at conditions where the potential for power extraction is higher would yield a superior overall turbine efficiency. For this application, the available power is computed assuming an isentropic expansion to the downstream pressure. Its trend over the pulsating period is presented in Fig. 13, highlighting a remarkably superior power potential when greater inlet total temperatures and pressures are observed. Based on these considerations, the design boundary conditions are selected to be those for a time of 0.02 s and are shown in Table 3. This operating point corresponds to a pressure ratio of 9, balancing efficiency across high- and low-pressure operating conditions. Additionally, the design point selection ensures a balanced distribution of the available work over the pulsating period, with 44% and 56% of the total available work distributed before and after a time of 0.02 s, respectively. In view of the preliminary nature of the presented system assessment, no optimization process was performed to confirm that the selected design point ensures the highest possible average efficiency over the pulsation.

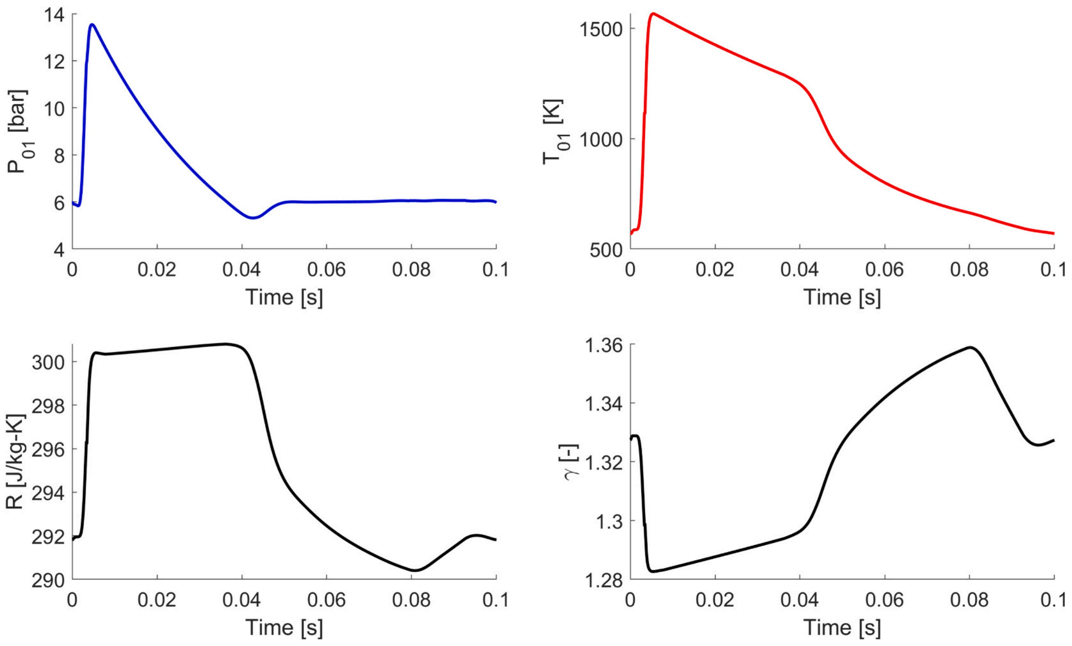

Fig. 12. Turbine inlet boundary conditions for a pulsating period.

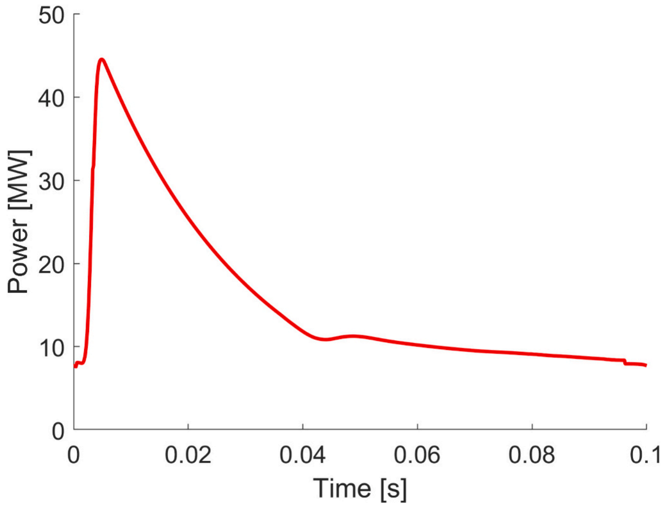

Fig. 13. Available turbine power over a pulsating period.

Table 3
Turbine design boundary conditions.

P_{01} [bar]	T_{01} [K]	γ [−]	**R** [J/kg-K]
9.02	1422	1.29	300.5

4.2. *Turbine architecture and geometry*

In the definition of the turbine architecture, a fundamental step is the selection of the number of stages, which is mainly driven by the pressure ratio. As previously discussed, the pressure ratio in this application presents an acute variation, ranging from 13.5 to 6. The turbine must be able to handle all pressure ratios; hence, for this analysis, the peak pressure ratio (13.5) is the driving factor. Considering an equally distributed pressure ratio across all stages, the individual stage pressure ratio can be determined. For a 2-stage turbine, the stage pressure ratio would be 3.67, whereas for a 3-stage configuration, it would drop to 2.38. Acknowledging that the pressure ratio of a highly loaded transonic turbine is in the order of three [17], a three-stage turbine architecture is considered as most suitable for the current application. To minimize complexity and mechanical integration, all stages are set to be driven by the same shaft.

To expedite the process and to ensure a functional design, an existing turbine geometry is chosen as the basis for the design. The TATEF turbine is a transonic stage with elevated efficiency and power extraction and has been studied in depth computationally and experimentally [16,17,24]. As a result, it is selected as the first turbine stage for this application. Considering the complexity and resources required for the three-dimensional design and assessment of an axial turbine stage, the use of the same TATEF turbine geometry is explored for the second and third stages.

To adapt the stage design to the flow conditions provided by the upstream turbine row, the vane endwalls on the second and third stages are modified. This is part of the conventional design procedure used historically in steam turbines, where the need for a large number of stages motivated the design of a single stage that could be repeated only with adjustments in the channel height [25,26]. This process has also been used to accommodate wider ranges of inlet Mach number operation in turbines for the integration of pressure gain technologies [23,27]. The process starts by retrieving the inlet total pressure, Mach number, and the tangential flow angle at the turbine stage inlet ($P_{0,in}, M_{in}, \alpha_{in}$), from the solution of the preceding turbine row. The Mach number exiting the vane is a design parameter and is known (M_{out}). The tangential flow angle at the vane outlet (α_{out}) is set equal to its design operating value. This may vary depending on the flow incidence at the inlet of the vane row; nonetheless it is deemed reasonable for the purpose of preliminary estimates. No work is extracted on the vane row; thus, the row inlet and outlet total temperature are considered equal. The outlet total pressure ($\boldsymbol{P_{0,out}}$) is calculated using turbine loss predictive models [28]. Given all these metrics, the required vane outlet area (A_{out}) can be solved employing mass conservation (Eq. 9). From there, the vane outlet channel height (H_{out}) is retrieved via Eq. 11.

$$A_{out} = \frac{A_{in} p_{0,in} D_{in}}{p_{0,out} D_{out}} \tag{9}$$

$$D = \frac{M}{\left(1 + \frac{\gamma - 1}{2} M^2\right)^{\frac{\gamma+1}{2(\gamma-1)}}} \tag{10}$$

$$H_{out} = \frac{A_{out}}{2\pi \cdot r_{mid,out} \cdot \cos(\alpha_{out})} \tag{11}$$

The endwall contour geometry used to increase the channel height from the vane inlet to the outlet is the result of an optimization conducted by Grasa et al. [23]. The geometry provides an intense level of diffusion while minimizing length and pressure losses and is tailored for fully developed boundary layers. To preserve the original endwall shape, the geometry is non-dimensionalized as a function of the passage length and radius, so that it can be applied to the design of the second and third stages. It is worth noting that due to the growth in channel height along the vane, the aspect ratio of the vane and blade rows does not remain equal to that of the original TATEF turbine stage, which may introduce minor deviations in the performance predictions. However, all other relevant non-dimensional parameters that define the vane and blade row geometries remain unaltered in all three stages.

4.3. *Turbine sizing*

To define the dimensions of all turbine stages and obtain preliminary estimates of performance, a 0D tool is developed. This reduced-order approach provides rapid solutions, allowing fast design iterations and the identification of the main design trends. Nevertheless, its ability to predict off-design performance and efficiency depends significantly on the turbine loss models in use. Hence, the solver is only intended to be used for the turbine sizing and estimates of performance at on-design conditions. A more comprehensive analysis at on- and off-design conditions is conducted afterwards, using 3D Reynolds-Averaged Navier-Stokes (RANS) simulations. The design inputs to the 0D tool are listed in Table 4. The selected vane outlet Mach numbers for all stages range between 0.9 and 0.95. These values were selected to ensure adequate flow incidences to their respective downstream rotor rows while preserving the transonic nature of the TATEF vane. The discrepancy between the chosen outlet Mach number and the TATEF vane design value of 1.03 [17] may introduce minor errors in the 0D performance predictions, due to differences in loss mechanisms across the vane. Regarding the Reynolds number, the metrics obtained at the vane outlet based on the chord length at mid-span range from $1.35 \cdot 10^6$ for the first stage to $8 \cdot 10^5$ for the third stage, close to the design Reynolds of the TATEF vane of 10^6. As a result, the differences in Reynolds number are not expected to induce considerable deviations in the performance estimates. The selected turbine speed ensures a 1st stage rotor inlet angle

Table 4
0D tool design variables.

Design variable	Value
1st stage vane outlet Mach number	0.95
2nd stage vane outlet Mach number	0.9
3rd stage vane outlet Mach number	0.9
Turbine speed	10,100 rpm

equal to the TATEF turbine rotor design condition [17]. The tool solves iteratively for the flow conditions at different locations until the desired downstream static pressure is attained.

The turbine loss predictions used for the vane and blade rows are based on previous numerical and computational studies [16] and the models outlined by Wei [28]. For adequate turbine row pressure loss estimates, it is vital to consider the flow incidence at the row inlet, given its impact on the loss mechanisms, particularly for positive incidence [27,29,30]. In turbomachinery, flow incidence is defined as the difference between the inlet flow angle and the row design metal angle, and it can be understood as the angle of attack on the airfoil. As a result of the overall favorable pressure gradient, axial turbine rows can operate over a wide range of positive and negative incidence without experiencing stall or surge, as opposed to compressors. The incidence at all row inlets is expected to vary over the pulsating period; nonetheless, at on-design conditions, the aim is to keep all incidences below ±15°. Table 5 summarizes the inlet flow incidence to each row predicted by the 0D tool at on-design conditions only. Except for the 2nd stage vane row, all values lie within the predefined incidence bounds for all rows, indicating that the overall pressure loss across the turbine may be well estimated at on-design conditions. Due to the modeling limitations in the 0D tool, the incidence levels over the pulsating period and their impact on the turbine efficiency are assessed via 3D RANS simulations.

The meridional view of the three-stage axial turbine is illustrated in Fig. 14. The first stage is highlighted in blue, with the vane (stationary) and blade (rotating) rows, in that order. The second and third stages are located downstream, highlighted in red. As previously discussed, the hub and shroud endwalls of the second and third-stage vane rows are altered with respect to the first stage.

4.4. Aerodynamic turbine response to pulsating inlet conditions

The turbine inlet conditions vary over the pulsating period, introducing temporal fluctuations in the main flow quantities. To determine whether fully time-resolved simulations are required, the degree of unsteadiness can be assessed through the reduced frequency, defined in Eq. 12. This non-dimensional parameter, equivalent to the Strouhal number, relates the excitation frequency at the turbine inlet to the convective response frequency downstream [14,31]. Low reduced frequencies indicate that the flow is convected through the machine much faster than the inlet conditions evolve, leading to a quasi-steady behavior. Under these circumstances, the flow field can be accurately captured through a sequence of steady-state simulations without significant loss of fidelity.

$$\bar{f} = \frac{f}{U_{1,ax}/L} \tag{12}$$

Sousa et al. [31] compared unsteady and quasi-steady simulations of turbines under pulsating supersonic inlet conditions. For reduced frequencies below 0.1, both approaches yielded nearly identical mean and peak total pressure and temperature distributions. Similarly, Liu et al. [14] reported that for reduced frequencies under 0.1, turbine efficiency decreased by less than one percentage point relative to steady results, while higher frequencies ($0.1 < \bar{f} < 1$) led to noticeable efficiency degradation.

In the present configuration, the excitation frequency of 10 Hz, combined with the turbine geometry and inlet velocity, results in reduced frequencies of 0.058 (using inlet velocity) and 0.039 (using mean axial velocity). These values fall well within the quasi-steady regime, indicating that the unsteady contribution to the main flow variables is minimal. Consequently, the turbine response is resolved using a series of steady-state simulations for multiple points along the inlet profile, achieving a suitable balance between computational efficiency and physical fidelity.

Table 5
Predicted row inlet flow incidences at on-design conditions.

Row	Incidence [deg]
1st stage blade inlet	5
2nd stage vane inlet	26
2nd stage blade inlet	−2
3rd stage vane inlet	−11
3rd stage blade inlet	−6

4.5. Computational tools used for the 3D turbine evaluation

To more accurately predict and analyze the turbine performance at different instances along the pulsating inlet period, the 3D RANS equations are solved using the Numeca FineTurbo suite. The solver's capability to predict the aerothermal field on a high-pressure turbine in a fully rotating environment has been experimentally validated [32], from De Maesschalck et al., presents the isentropic Mach number and Nusselt number distributions at the rotor mid-span, demonstrating a good agreement overall between the CFD and the experiments.

Uniform total pressure and total temperature are imposed at the inlet, together with a turbulent intensity level of 5% and a turbulent length scale of 1 mm. Static pressure is set at the domain outlet, with sea-level atmospheric pressure in all cases. The fluid is modeled as a perfect gas with constant specific heats; however, the specific heats in each simulation are adjusted according to each specific condition over the pulsation period, accounting for the gas property variations shown in Fig. 12. For single-stage simulations, the fluid properties are computed at the inlet. For multi-stage simulations, the specific heats would change across the turbine due to the power extraction and total temperature drop observed in the turbine rotors. This effect is accounted for by employing an average specific heat ratio, based on the expected inlet and outlet values obtained from the 0D tool. This way, any deviations in the specific heat ratio are abated, minimizing potential discrepancies in the results. The vane-blade and blade-vane interfaces employ a full non-matching mixing plane approach, following Numeca's recommendation [33]. All turbine stages are shrouded, resulting in no gap between the rotor tip and the shroud endwall. Tip leakage flows are known to have a noticeable impact on the efficiency of high-pressure turbines, and the flow topology can vary significantly with tighter tip clearances [34]. All walls are treated as no-slip and adiabatic, and the two-equation k-ω SST model provides the turbulence closure. The numerical model employs a second-order spatial discretization approach, with a central differencing scheme. Numerical convergence is monitored via the numerical residuals and the evolution of some fundamental metrics, namely the torque, total-to-total pressure ratio, and total-to-total isentropic efficiency. The convergence criteria consisted of residuals levels equal to or below 10^{-3} for all transport equations, together with stable values of the aforementioned metrics, only allowing oscillations of an amplitude below 0.1% of the mean value.

The computational grid is generated via Autogrid5 from Numeca, which is particularly tuned for turbomachinery configurations, providing high-quality, structured meshes. The first cell height is set to 1 μm, ensuring a $y+$ below 1 in the entire domain and resolving the viscous sublayer. The grid settings were selected from the grid independence study presented in [23], which was executed for the transonic TATEF vane with the aforementioned endwall contour geometry, providing a very similar design case to that discussed in this manuscript. The medium grid configuration, as presented in [23], exhibited differences below 0.09% and 0.14% in the outlet mass-flow averaged total pressure and flow angle, and was able to accurately capture the spanwise flow angle distribution, as shown in Fig. 16. As a result, the same grid configuration has been employed in this analysis, yielding a full turbine cell count of 15.2 million.

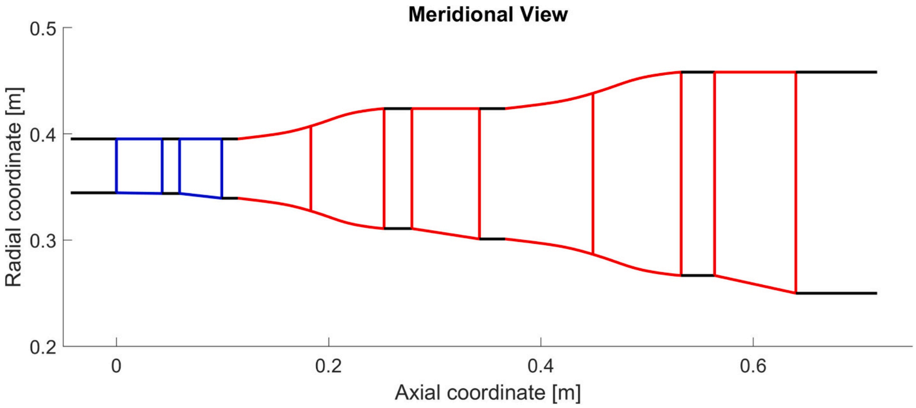

Fig. 14. Three-stage axial turbine design – Meridional view.

5. Overall engine performance

5.1. Turbine response

The 0D tool is employed to size the turbine and to obtain preliminary performance estimates. To confirm the validity of the turbine sizing, three-dimensional simulations of each individual turbine stage were conducted at on-design conditions. For this purpose, individual-stage simulations were preferred over a full turbine analysis, since the boundary conditions can be set as those used in the sizing tool, providing a fairer comparison to the 0D estimates. Additionally, given the smaller computational cost of individual-stage calculations, any potential numerical errors can be troubleshooted more easily. Table 6 presents multiple performance metrics of each of the three turbine stages at on-design conditions, obtained via the 0D tool and 3D RANS calculations. Given the inherent limitations of a zero-dimensional tool to model a highly three-dimensional flow field, the expected confidence interval on the 0D tool results is +/− 10%. By contrast, the 3D RANS code is expected to be in the order of +/− 2% for aerodynamic metrics, as presented in Fig. 15 for previous experimental validations [32]. In view of the satisfactory level of agreement in the individual turbine stage performance predictions, the full three-stage turbine is evaluated via 3D RANS. Fig. 17 compares the blade loading of the 3rd stage rotor row at mid-span with that of the original TATEF turbine [17]. Despite the presence of positive flow incidence and a non-uniform outflow from the preceding turbine stages, the similarity in the isentropic Mach number distributions along the suction side and pressure side of the blade demonstrates that the turbine behaves as intended, even at the most downstream rotor row.

Once adequate performance is demonstrated at on-design conditions, the turbine response over the pulsating period is analyzed using 3D RANS simulations. Due to the low reduced frequency, the turbine performance along the inlet pulsating period can be accurately assessed as a sequence of steady-state calculations. In total, eight different conditions have been selected, as illustrated in Fig. 18. The distribution of the selected conditions along the pulsating period features a finer resolution over the region with increased potential for power extraction, highlighted in Fig. 13. As expected, the turbine exhibits a high efficiency near its design point. Moreover, it retains that level of efficiency for a considerable portion of the pulsating period. In addition, the conditions of greatest efficiency align with those of largest power extraction, yielding an average efficiency over the pulsating period of 90% (Eq. 13), demonstrating the suitability of an ad-hoc axial turbine design to efficiently harness the work potential of a pressure gain combustor.

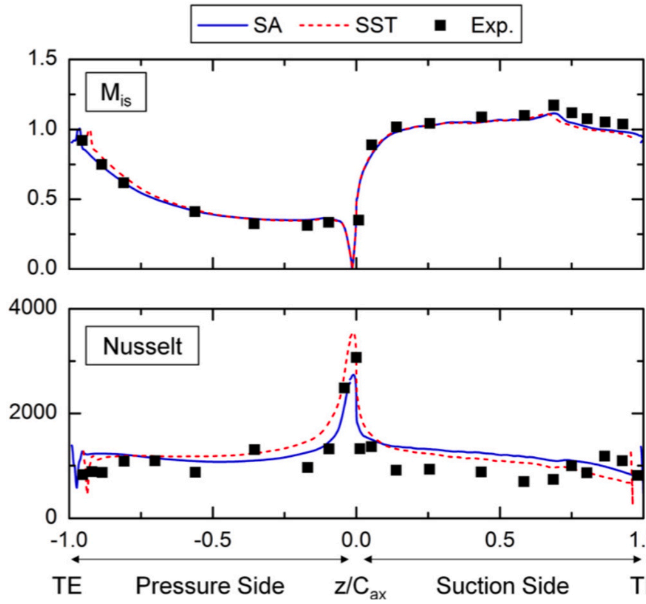

Fig. 15. Solver validation – Comparison of experimental and numerical isentropic Mach number and Nusselt number distributions [32].

$$\eta_{tt,av} = \frac{\int_0^{period} \dot{W}_{real}(t)\cdot dt}{\int_0^{period} \dot{W}_{ideal}(t)\cdot dt} \tag{13}$$

Table 6
Turbine performance comparison – 0D tool vs 3D RANS.

# Stage	Analysis	$M_2[-]$	$M_3[-]$	$\beta_3[^\circ]$	$\alpha_3[^\circ]$	$P_{03}[bar]$	$\dot{W}[MW]$	$\dot{m}[kg/s]$
1	0D Tool	0.95	0.47	−62	−26	3.93	8.8	29.3
	3D RANS	1.02	0.4	−63	−21	3.82	9.06	29.8
2	0D Tool	0.9	0.3	−62	11	2.03	5.9	29.3
	3D RANS	0.87	0.3	−62	16	2.05	5.45	28.8
3	0D Tool	0.9	0.29	−62	24	1.07	5.03	29.3
	3D RANS	0.84	0.34	−61	26	1.11	4.67	27.8

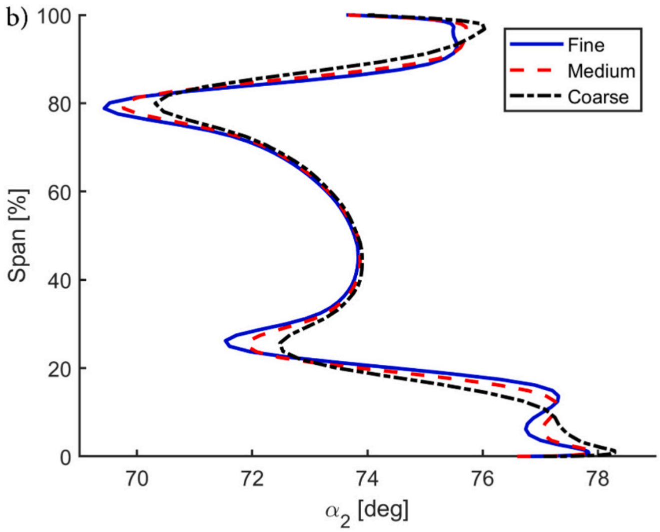

Fig. 16. Grid independence analysis – Outlet angle radial distribution [23].

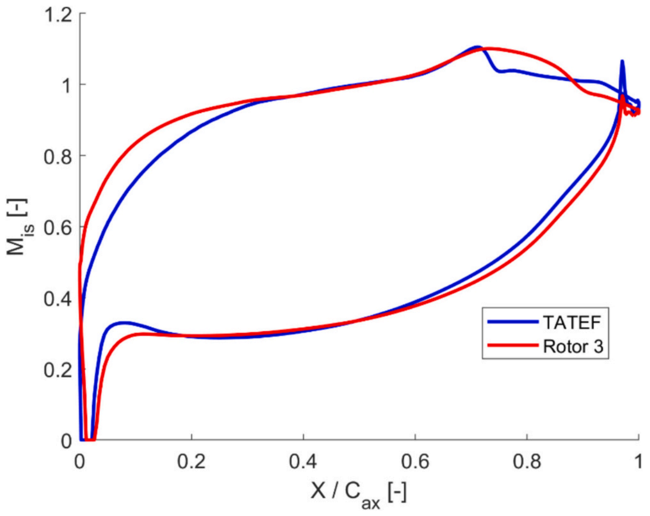

Fig. 17. Rotor blade loading comparison - Isentropic Mach number distribution at 50% span at on-design conditions.

5.2. Engine cycle analysis

For an accurate representation of the system's behavior, it is essential to analyze and simulate the entire cycle rather than considering the combustor and turbine as separate components. Thus, the scaled-up 1D combustor model was modified to incorporate turbine efficiency variations during a pulsation, as derived from turbine simulations. As discussed in Section 3.4, the layout of the scaled-up 1D model (Fig. 11) was adjusted to ensure proper coupling with the turbine while adhering to scaling laws. The same layout was adapted to test the entire cycle simulation. Modifying the structure of components downstream of the combustor may affect the boundary conditions at the turbine inlet and, consequently, influence the computed turbine efficiency trend. In the *Simple Turbine* template, efficiency is imposed as a fixed value or a time- or angle-dependent trend. Nonetheless, the full-system analysis reveals that the total pressure, total temperature, and mass flow trends at the turbine inlet showed an almost exact match with the original values used for the turbine design, with the standard deviation between both inlet profiles being respectively $7.87{\cdot}10^{-3}$ bar, 4.69 K, and $1.23{\cdot}10^{-3}$ kg/s. This result not only validates the appropriate use of the time-dependent efficiency but also confirms the scaling strategy's validity and the turbine design approach. With this enhancement, the 1D model can now effectively simulate the full operational cycle of the pulsating combustor coupled with a downstream turbine.

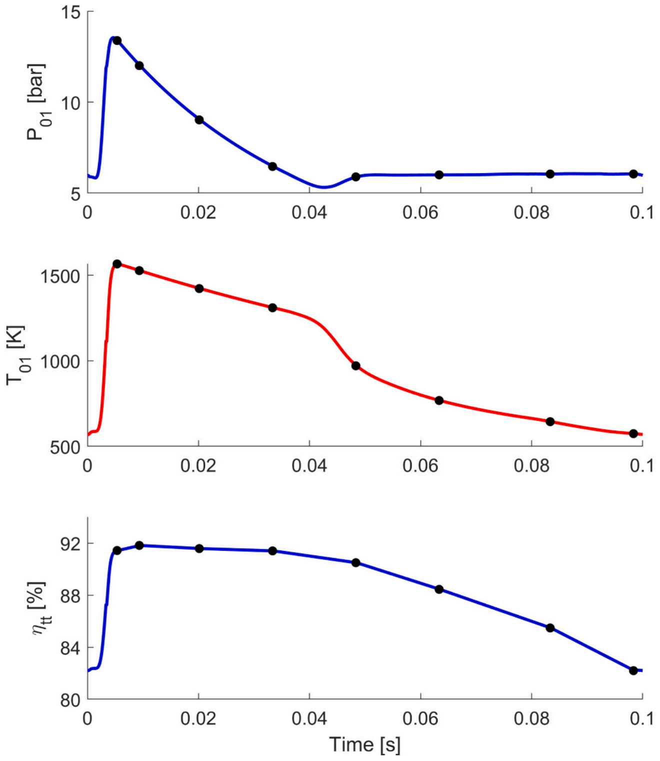

Fig. 18. Turbine performance over the inlet pulsating period.

To compare the performance of the proposed system to existing gas turbines and to other potential pressure gain technologies, such as rotating detonation engines (RDE), a simplified zero-dimensional model was used to simulate a Brayton cycle. To ensure a proper comparison between the cycles, both employed the same pressure ratio and isentropic efficiency in the compression phase, as well as an isentropic turbine efficiency of 0.9, determined from the previous modeling. Two scenarios were considered regarding pressure gain, one with a combustor total pressure loss of 10% and the second with a net total pressure gain of 5%. These metrics were selected based on the RDE experimental performance data presented so far in the open literature [35], with the best reported performance being in the order of 3 to 5% pressure loss. Table 7 summarizes the cycle performance across the various cases analyzed.

With a fuel power input of 18.75 MW and a net power output of 6.02 MW, the resulting cycle efficiency reaches 32.09%, an improvement of 2.29 percentage points over a traditional Brayton cycle. This represents a significant enhancement compared to conventional systems, highlighting the potential for greater fuel savings, lower emissions, and improved overall performance. Additionally, the deflagrative-based PGC notably outperforms an RDE under an optimistic performance

Table 7
Summary of cycle efficiency in the cases examined.

Case	Q_{in} [MW]	η_{cycle} [%]
PGC – 10% combustor pressure loss	18.75	27.02
Conventional Brayton	18.75	29.80
PGC – 5% combustor pressure gain	18.75	30.79
Deflagrative-based PGC	18.75	32.09
Deflagrative-based PGC – no Fuel Losses (FL)	18.54	32.45
Deflagrative-based PGC – no Heat Losses (HL)	17.62	34.15
Deflagrative-based PGC – no FL and HL	17.41	34.55

scenario of 5% pressure gain, with a cycle efficiency 1.3 percentage points higher. Apart from calculating the overall cycle efficiency, the model also identifies existing sources of loss. It is important to note that the model is based on experimental data from a test bench equipped with a prototype-level combustor. One of the key objectives in developing the 1D combustor model was to identify loss sources and pinpoint potential areas of improvement, helping to optimize performance and enhance future design. Two main loss sources were identified. Of the total fuel power injected, 1.1% is lost due to unburned fuel exiting the chamber, while 6.0% is lost as heat. Both losses significantly impact cycle efficiency and can potentially be reduced in future development phases. Fuel losses can be minimized by adjusting the injection timing and duration during the intake phase. Heat losses, on the other hand, can be reduced by enhancing the insulation or recovering heat to preheat the incoming fresh air. If these losses are eliminated, the cycle efficiency would reach 34.55%, marking a substantial improvement.

6. Conclusion

This study presented a comprehensive numerical investigation of a pistonless deflagration-based hydrogen-fueled Pressure Gain Combustor integrated with a downstream axial turbine. The principal objective was to establish a validated simulation framework that accurately captures the dynamics of the combustor and enables a full-system performance analysis under pulsating flow conditions. The main findings of the study are summarized below:

- The one-dimensional combustor model demonstrated that the transient thermodynamic behavior of a deflagration-based PGC can be reproduced with sufficient accuracy for system-level analysis. The calibrated model captured the main dynamics over a pulsation cycle, confirming that a reduced-order, one-dimensional approach can reliably describe the operational characteristics of the pulsating combustor for the investigated configuration.
- The dedicated axial turbine was shown to operate efficiently under pulsating inlet conditions, with only limited sensitivity to unsteady pressure and temperature fluctuations. The use of transient combustor outlet quantities as turbine inlet boundary conditions preserved the essential unsteady features of the flow, enabling meaningful assessment of turbine performance under realistic operating conditions. Despite the variations imposed by the combustor, the turbine achieved a time-average efficiency of approximately 90% over a pulsation cycle. This result demonstrates that high turbine efficiency is achievable even when coupled to a pulsating PGC, supporting the practical feasibility of such integrations.
- A full-system simulation model was then constructed, integrating the validated combustor and turbine models to enable cycle-level evaluations under realistic operating conditions. The analysis revealed a cycle efficiency of 32.1%, representing a 7.7% gain over traditional Brayton cycles with constant pressure combustion. In addition, the analysis identified two key loss mechanisms that currently limit further performance gains: fuel burn inefficiencies (1.1% of input power) and thermal losses to the surroundings (6.0%). These findings provide a clear roadmap for the next phase of research, where improved thermal management and combustion optimization strategies can be employed to push efficiency levels toward the theoretical upper bound of 34.55%.

From a modeling perspective, the simulation framework developed here offers multiple advantages. It provides a realistic yet computationally efficient alternative to high-fidelity 3D simulations, which are often prohibitively expensive for parametric studies or early-stage design iterations. While CFD remains critical for capturing fine-scale turbulence and mixing phenomena, the 1D tool presented here serves as an excellent complement, particularly for identifying design trends, evaluating control strategies, and enabling system-level optimization.

Another key contribution of this work lies in the demonstration of a system-level approach to evaluating PGCs. Unlike isolated component studies that only assess combustion chamber or turbine behavior individually, this study highlighted the importance of integrated system analysis. The direct coupling of combustor and turbine models enabled an assessment of unsteady interactions, loss propagation, and transient response—all critical to the reliable operation of advanced gas turbine engines. Moreover, the integration of such PGC systems with existing turbomachinery frameworks offers an evolutionary path for adopting pressure gain technology without requiring a complete reengineering of the engine architecture.

The results presented in this work are specific to the investigated combustor and to a fixed operating condition defined by the experimental campaign. Accordingly, the present work should be interpreted as a first order validation of the proposed concept. Further investigations will be required to assess the predictive capability of the model under off-design and alternative operating conditions, and to evaluate its robustness in capturing deviations from the reference case. Nevertheless, the modeling methodology presented herein is not limited to the system analyzed. With appropriate adjustments to geometric representations, boundary conditions, and operating logic, the proposed approach can be extended to the modeling of other deflagrative-based quasi-Constant Volume Combustors. In this sense, the present work provides a structured and computationally efficient methodology for the system-level analysis of deflagration quasi-CVC. It provides valuable insights for the design and optimization of next-generation power generation technologies, supporting the broader adoption of pressure gain combustion in clean and efficient energy systems.

CRediT authorship contribution statement

C. Tempesti: Writing – review & editing, Writing – original draft, Visualization, Software, Methodology, Investigation, Formal analysis, Data curation. **S. Grasa:** Writing – review & editing, Writing – original draft, Software, Methodology, Investigation, Formal analysis. **L. Romani:** Writing – review & editing, Supervision. **F. Ciccateri:** Project administration, Conceptualization. **G. Ferrara:** Supervision. **G. Paniagua:** Writing – review & editing, Supervision, Conceptualization.

Declaration of competing interest

The authors declare the following financial interests/personal relationships which may be considered as potential competing interests: Fabio Ciccateri has patent issued to Finno Exergy Oy. If there are other authors, they declare that they have no known competing financial interests or personal relationships that could have appeared to influence the work reported in this paper.

Data availability

Data will be made available on request.

References

[1] H.J. Salminen, F. Ciccateri, T. Ijäs, O. Ulmala, M. Mikulski, Experimental demonstration of a novel deflagration-based pressure gain combustion technology. *AIAA propulsion and energy 2020 forum*, 1–8, 2020, https://doi.org/10.2514/6.2020-3871.

[2] C. Tempesti, L. Romani, M. Ciampolini, O. Hakuri, F. Ciccateri, G. Ferrara, Experimental methodology for the characterization of a hydrogen-fuelled pressure gain combustor, J. Phys. Conf. Ser. 2648 (1) (2023), https://doi.org/10.1088/1742-6596/2648/1/012062.

[3] M.R. Nalim, Thermodynamic limits of work and pressure gain in combustion and evaporation processes, J. Propuls. Power 18 (6) (2002) 1176–1182, https://doi.org/10.2514/2.6076.

[4] P. Stathopoulos, Comprehensive thermodynamic analysis of the Humphrey cycle for gas turbines with pressure gain combustion, Energies 11 (12) (2018) 3521, https://doi.org/10.3390/en11123521.

[5] L. Labarrere, T. Poinsot, A. Dauptain, F. Duchaine, M. Bellenoue, B. Boust, Experimental and numerical study of cyclic variations in a constant volume combustion chamber, Combust. Flame 172 (2016) 49–61, https://doi.org/10.1016/j.combustflame.2016.06.027.

[6] N. Detomaso, D. Laera, P. Pouech, F. Duchaine, T. Poinsot, Large Eddy simulation of a Pistonless constant volume combustor: a new concept of pressure gain combustion, J. Eng. Gas Turbines Power 145 (2) (2023) 021025, https://doi.org/10.1115/1.4056018.

[7] C. Xisto, O. Petit, T. Grönstedt, A. Rolt, A. Lundbladh, G. Paniagua, The efficiency of a pulsed detonation combustor–axial turbine integration, Aerosp Sci Technol 82–83 (2018) 80–91, https://doi.org/10.1016/j.ast.2018.08.038.

[8] P. Berndt, R. Klein, Modeling the kinetics of the Shockless explosion combustion, Combust. Flame 175 (2017) 16–26, https://doi.org/10.1016/j.combustflame.2016.06.029.

[9] N. Neumann, M. Asli, N. Garan, D. Peitsch, P. Stathopoulos, A fast approach for unsteady compressor performance simulation under boundary condition caused by pressure gain combustion, Appl. Therm. Eng. 196 (2021) 117223, https://doi.org/10.1016/j.applthermaleng.2021.117223.

[10] M. Asli, N. Garan, N. Neumann, P. Stathopoulos, A robust one-dimensional approach for the performance evaluation of turbines driven by pulsed detonation combustion, Energ. Conver. Manage. 248 (2021) 114784, https://doi.org/10.1016/j.enconman.2021.114784.

[11] J. Sousa, G. Paniagua, E. Collado Morata, Thermodynamic analysis of a gas turbine engine with a rotating detonation combustor, Appl. Energy 195 (2017) 247–256, https://doi.org/10.1016/j.apenergy.2017.03.045.

[12] P. Gallis, D. Misul, S. Salvadori, M. Bellenoue, B. Boust, Development and Validation of a 0-D/1-D Model to Evaluate Pulsating Conditions from a Constant Volume Combustor, *Proceedings of the Joint Meeting of International Workshop on Detonation for Propulsion (IWDP) and International Constant Volume and Detonation Combustion Workshop (ICVDCW),* Berlin, Germany, 2022.

[13] P. Gallis, D.A. Misul, B. Boust, M. Bellenoue, S. Salvadori, Development of 1D model of constant-volume combustor and numerical analysis of the exhaust nozzle, Energies 17 (5) (2024) 1191, https://doi.org/10.3390/en17051191.

[14] Z. Liu, J. Braun, G. Paniagua, Integration of a transonic high-pressure turbine with a rotating detonation combustor and a diffuser, International Journal of Turbo and Jet Engines 40 (1) (2023) 1–10, https://doi.org/10.1515/tjj-2020-0016.

[15] Z. Liu, J. Braun, G. Paniagua, Thermal power plant upgrade via a rotating detonation combustor and retrofitted turbine with optimized endwalls, Int. J. Mech. Sci. 188 (2020) 105918, https://doi.org/10.1016/j.ijmecsci.2020.105918.

[16] N. Mushtaq, G. Persico, P. Gaetani, The role of endwall shape optimization in the design of supersonic turbines for rotating detonation engines, J. Turbomach. 145 (8) (2023), https://doi.org/10.1115/1.4062277.

[17] R. Dénos, T. Arts, G. Paniagua, V. Michelassi, F. Martelli, Investigation of the unsteady rotor aerodynamics in a transonic turbine stage, J Turbomach 123 (1) (2001) 81–89, https://doi.org/10.1115/1.1314607.

[18] GT-SUITE, Engine Performance Application Manual, Version, 2022. Gamma Technologies.

[19] GT-SUITE, Flow Theory Manual, Version, 2022. Gamma Technologies.

[20] K. Deb, H. Jain, An evolutionary many-objective optimization algorithm using reference-point-based nondominated sorting approach, part I: solving problems with box constraints, IEEE Trans. Evol. Comput. 18 (4) (2014) 577–601, https://doi.org/10.1109/tevc.2013.2281535.

[21] D. Hadka, MOEA Framework User Guide. Version 2.6. http://www.moeaframework.org/, 2015.

[22] S. Regitz, N. Collings, Fast response air-to-fuel ratio measurements using a novel device based on a wide band lambda sensor, Meas. Sci. Technol. 19 (7) (2008), https://doi.org/10.1088/0957-0233/19/7/075201.

[23] S. Grasa, G. Paniagua, Design and characterization of highly diffusive turbine vanes suitable for transonic rotating detonation combustors, Int. J. Turbomach. Propuls. Power 9 (2) (2024), https://doi.org/10.3390/ijtpp9020018.

[24] C. Sieverding, T. Arts, T. Denos, F. Martelli, Investigation of the flow field downstream of a turbine trailing edge cooled nozzle guide vane, J Turbomach 118 (1996) 291–300, https://doi.org/10.1115/1.2836639.

[25] N. Baines, Turbine Design and Analysis (1st ed.). (N C Baines), 2019.

[26] R.H. Aungier, Turbine aerodynamics: axial-flow and radial-flow turbine design and analysis, ASME Press, 2006, https://doi.org/10.1115/1.802418.

[27] S. Grasa, G. Paniagua, Design, multi-point optimization, and analysis of diffusive stator vanes to enable turbine integration into rotating detonation engines, J. Turbomach. 146 (11) (2024), https://doi.org/10.1115/1.4065424.

[28] N. Wei, Significance of Loss Models in Aerothermodynamic Simulation for Axial Turbines, Doctoral Thesis, Royal Institute of Technology, 2000.

[29] A.B. Mcvetta, P.W. Giel, G.E. Welch, Aerodynamic Investigation of Incidence Angle Effects in a Large Scale Transonic Turbine Cascade [Online]. Available, http://www.sti.nasa.gov, 2014.

[30] D.G. Ainley, G.C.R. Mathieson, An Examination of the Flow and Pressure Losses in Blade Rows of Axial-Flow Turbines, London, 1951.

[31] J. Sousa, G. Paniagua, J. Saavedra, Aerodynamic response of internal passages to pulsating inlet supersonic conditions, Comput. Fluids 149 (2017) 31–40, https://doi.org/10.1016/j.compfluid.2017.03.005.

[32] C. de Maesschalck, S. Lavagnoli, G. Paniagua, Blade tip carving effects on the aerothermal performance of a transonic turbine, J. Turbomach. 137 (2) (2015), https://doi.org/10.1115/1.4028326.

[33] Numeca International, User Guide FINE/Turbo 15.1, Brussels, 2020 [Online]. Available, www.numeca.com.

[34] C. de Maesschalck, S. Lavagnoli, G. Paniagua, N. Vinha, Aerothermodynamics of tight rotor tip clearance flows in high-speed unshrouded turbines, Appl. Therm. Eng. 65 (1–2) (2014) 343–351, https://doi.org/10.1016/j.applthermaleng.2014.01.015.

[35] A. Ruan, R.M. Gejji, E. Bach, C.D. Slabaugh, G. Paniagua, Effect of Geometric and Flow Parameters on Hydrogen-Air Rotating Detonation Combustor Operability and Performance, AIAA SciTech 2025 Forum, 2025 doi: https://doi.org/10.2514/6.2025–1774.